AGU PUBLICATIONS

JGR

Journal of Geophysical Research: Oceans

RESEARCH ARTICLE

10.1002/2015JC011449

Key Points:
- A new model of the Bering Sea in spring replicates a wide variety of phytoplankton/grazer metrics
- Total spring primary production is generally higher in warm years, but the relationship is indirect
- Ice cover, mixing, and advection control distinct aspects of bloom timing and magnitude

Correspondence to:
N. S. Banas,
neil.banas@strath.ac.uk

Citation:
Banas, N. S., J. Zhang, R. G. Campbell, R. N. Sambrotto, M. W. Lomas, E. Sherr, B. Sherr, C. Ashjian, D. Stoecker, and E. J. Lessard (2016), Spring plankton dynamics in the Eastern Bering Sea, 1971–2050: Mechanisms of interannual variability diagnosed with a numerical model, *J. Geophys. Res. Oceans*, *121*, doi:10.1002/2015JC011449.

Received 9 NOV 2015
Accepted 25 JAN 2016
Accepted article online 3 FEB 2016

Spring plankton dynamics in the Eastern Bering Sea, 1971–2050: Mechanisms of interannual variability diagnosed with a numerical model

Neil S. Banas[1], Jinlun Zhang[2], Robert G. Campbell[3], Raymond N. Sambrotto[4], Michael W. Lomas[5], Evelyn Sherr[6], Barry Sherr[6], Carin Ashjian[7], Diane Stoecker[8], and Evelyn J. Lessard[9]

[1]Department of Mathematics and Statistics, University of Strathclyde, Glasgow, UK, [2]Applied Physics Laboratory, Seattle, Washington, USA, [3]University of Rhode Island, Kingston, Rhode Island, USA, [4]LDEO, Palisades, New York, USA, [5]Bigelow Laboratory for Ocean Sciences, East Boothbay, Maine, USA, [6]College of Earth, Ocean, and Atmospheric Sciences, Oregon State University, Corvallis, Oregon, [7]Biology Department, Woods Hole Oceanographic Institution, Woods Hole, Massachusetts, USA, [8]Horn Point Laboratory, University of Maryland Center for Environmental Science, Cambridge, Maryland, USA, [9]School of Oceanography, University of Washington, Seattle, Washington, USA

Abstract A new planktonic ecosystem model was constructed for the Eastern Bering Sea based on observations from the 2007–2010 BEST/BSIERP (Bering Ecosystem Study/Bering Sea Integrated Ecosystem Research Program) field program. When run with forcing from a data-assimilative ice-ocean hindcast of 1971–2012, the model performs well against observations of spring bloom time evolution (phytoplankton and microzooplankton biomass, growth and grazing rates, and ratios among new, regenerated, and export production). On the southern middle shelf (57°N, station M2), the model replicates the generally inverse relationship between ice-retreat timing and spring bloom timing known from observations, and the simpler direct relationship between the two that has been observed on the northern middle shelf (62°N, station M8). The relationship between simulated mean primary production and mean temperature in spring (15 February to 15 July) is generally positive, although this was found to be an indirect relationship which does not continue to apply across a future projection of temperature and ice cover in the 2040s. At M2, the leading direct controls on total spring primary production are found to be advective and turbulent nutrient supply, suggesting that mesoscale, wind-driven processes—advective transport and storminess—may be crucial to long-term trends in spring primary production in the southeastern Bering Sea, with temperature and ice cover playing only indirect roles. Sensitivity experiments suggest that direct dependence of planktonic growth and metabolic rates on temperature is less significant overall than the other drivers correlated with temperature described above.

1. Introduction

The Eastern Bering Sea (EBS) hosts extremely rich pelagic and benthic fisheries and also experiences strong interannual variation in both fisheries recruitment and the underlying physics and plankton biology [*Hunt et al.*, 2011; *Coyle et al.*, 2011; *Stabeno et al.*, 2012a]. This paper uses a new planktonic ecosystem model to integrate diverse observations from The Bering Sea Project (BEST/BSIERP, Bering Ecosystem Study/Bering Sea Integrated Ecosystem Research Program: *Wiese et al.* [2012]) and to answer the question: What controls variation in spring primary production (in both magnitude and timing) across the range of warm and cold annual conditions seen over the past 40 years? This question is part of a larger class of problems in global change biology: the response of planktonic systems to multiple drivers; in particular, the response of high-latitude marine ecosystems to changing temperature, ice-linked phenology, and other mesoscale processes when the relationships among these processes are themselves changing. We use a new future model projection of temperature and ice cover in the 2040s to sketch one possible future for the Bering Sea, and to comment on the problem of prediction under multiple, highly correlated drivers.

1.1. Interannual Variation and Links From Climate to Food Webs

The EBS is a broad (>500 km) shelf system, divided by persistent fronts into inner (<50 m water depth), middle (50–100 m), and outer (100–200 m) domains [*Coachman*, 1986]. Seasonal ice cover is controlled by a balance of southward advection from Bering Strait and in situ melting and dispersion, and thus by a combination of wind

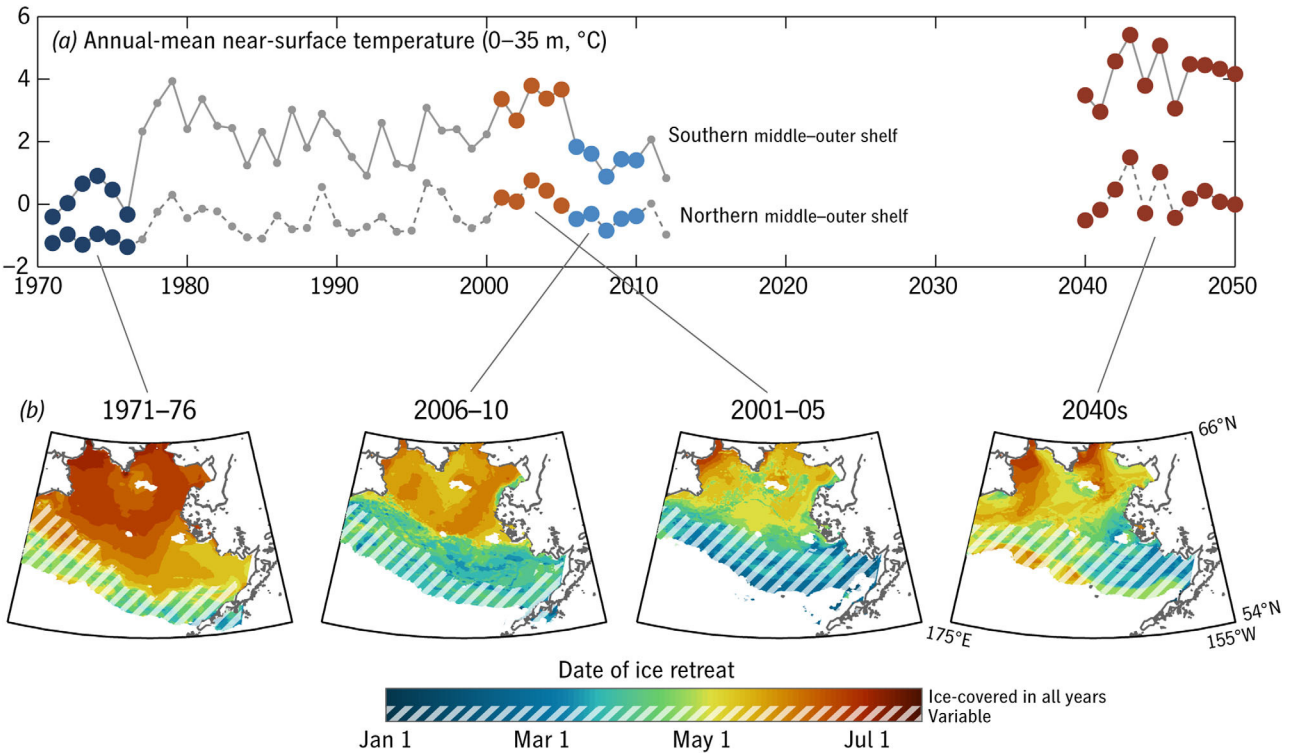

Figure 1. (a) Annual-mean temperature averaged over 0–35 m water depth on the EBS middle-outer shelf, from the BESTMAS model. Averages are shown for the northern (>60°N: dashed) and southern (<60°N: solid) shelves. (b) Annual-maximum ice cover and date of ice retreat (the last date on which ice cover > 10%) averaged over four contrasting sets of years (Figure 1a, colored dots, also from BESTMAS).

forcing and temperature [*Stabeno et al.*, 2012a]. The northern shelf (>60°N) consistently sees seasonal ice cover, while ice cover on the southern shelf is highly variable: at the long-term mooring site M2 (Figure 1) [*Stabeno et al.*, 2012a], the period of ice cover varied from several months to effectively zero among the years of the 2000s.

Hydrography and currents in the EBS respond strongly to variations in the strength and position of the Aleutian Low [*Danielson et al.*, 2011a] and other North Pacific-scale drivers [*Rodionov et al.*, 2007; *Danielson et al.*, 2011b]. The warm anomaly of the early 2000s and the cold anomaly of the late 2000s (Figure 1) have received much attention [e.g., *Grebmeier et al.*, 2006; *Coyle et al.*, 2011; *Sigler et al.*, 2014], largely because these anomalies left large imprints on fisheries recruitment and zooplankton composition. Large crustacean zooplankton were a much larger fraction of the late-summer mesozooplankton community on the southern shelf in cold years of the 2000s [*Eisner et al.*, 2014]. The pattern on the northern shelf was consistent with this, but both the environmental and the biological contrast there were much smaller. A reduction in large copepod and euphausiid abundance is thought to drive both bottom-up and top-down stresses on juvenile pollock and salmon [*Hunt et al.*, 2011; *Coyle et al.*, 2011].

Several factors could contribute to warm year/cold year variation in large zooplankton abundance at the end of the productive season: variation in total productivity of their phytoplankton and microzooplankton prey; direct temperature effects on summer growth and development and on winter metabolic losses; timing of prey availability and match/mismatch with the zooplankters' ontogenetic cycle. Prey productivity and timing can be further broken down into its pelagic and ice-algal components [*Cooper et al.*, 2013], and ice algae may be particularly important from a timing perspective [*Durbin and Casas*, 2014; *Daase et al.*, 2013]. A follow-on model study will consider this full array of factors linking climate to large zooplankton, whereas the present study is concerned with pelagic phytoplankton and microzooplankton production in spring (February–July), the most productive period of the year [*Stabeno et al.*, 2012a; *Sigler et al.*, 2014]. The model presented here was designed to answer the question: how much, and by what mechanisms, does environmental variation between cold and warm conditions affect phytoplankton and microzooplankton production and energy input into the pelagic and benthic food webs?

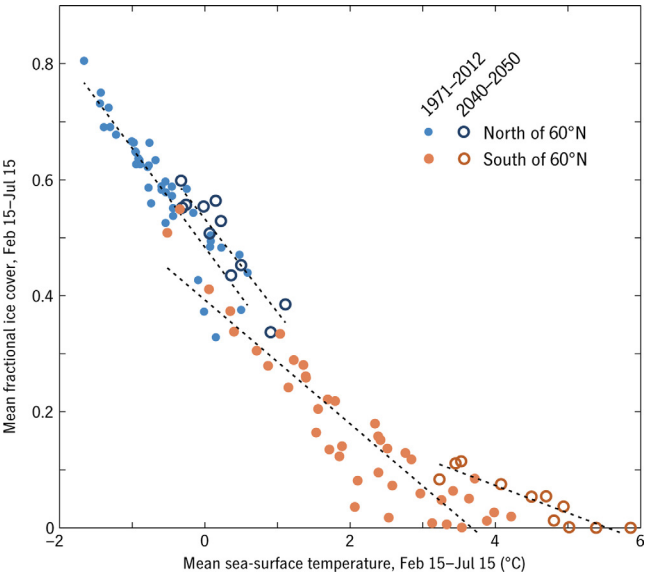

Figure 2. Relationship between ice cover and temperature, averaged 15 February to 15 July for the northern and southern middle-outer shelf separately, for each of the BESTMAS model years shown in Figure 1. Regression lines are shown for four subsets (north/south and hindcast/future).

Figure 1 shows the warm and cold years of the 2000s in the context of the even colder period of the early 1970s and the potentially even warmer conditions that could arrive by mid-century, according to a model hindcast/projection—described in detail below—using BESTMAS (Bering Ecosystem Study Ice-ocean Modeling and Assimilation System: *Zhang et al.* [2010a]). Average surface water temperature varies coherently between the northern and southern shelves (Figure 1a) and is accompanied by variation in ice cover (Figure 1b). Note that in the north, this is felt primarily as variation in ice-retreat timing of 1–2 month, whereas in the south, not only is the variation in timing even greater, but the extent of maximum ice cover varies latitudinally by hundreds of km as well. Ice cover regulates pelagic production via both light penetration and stratification. Note that in ice-free areas of the EBS, thermal stratification can be intense [*Stabeno et al.*, 2012b] but, counterintuitively, summer stratification is not well correlated with surface temperature [*Ladd and Stabeno*, 2012]. Nutrient availability depends on both stratification and horizontal transport [*Danielson et al.*, 2011a].

1.2. Multidecadal Variation

It is likely that as the earth, and high latitudes in particular, continue to warm over coming decades, this set of environmental drivers will not all change in familiar proportions. The multidecadal, anthropogenic shift in the thermodynamic budget of the region is a fundamentally different mechanism from the mesoscale atmospheric variability that drives interannual anomalies in temperature, ice cover, transport, and storminess, and thus we should not expect multidecadal trends in water temperature, ice cover, advective nutrient replenishment, and turbulent mixing to follow the same correlation lines as recent interannual variability. Indeed, the model projection used in this study (Figure 2; see section 2.1 below), depicts one possible future in which novel combinations of ice influence and mean temperature are commonplace by the 2040s, especially in the south.

The question then arises: as higher temperatures come to the EBS and other polar and subpolar regions, are the higher temperatures themselves likely to be the driver of crucial ecological shifts in the plankton, or important mainly as a proxy for correlated mechanisms (e.g., changes in ice-linked phenology or weather patterns)? A number of recent studies have argued for the former, drawing on the metabolic theory of ecology [*Brown et al.*, 2004] and related empirical studies to argue that differences in the temperature dependence of photosynthesis and respiration, or the net temperature responses of phytoplankton and their grazers, will lead to a tipping point for Arctic planktonic ecosystems with 5°C–6°C of additional warming [*Rose and Caron*, 2007; *Holding et al.*, 2013; *Alcaraz et al.*, 2014]. A model like the one constructed and evaluated here is well suited to testing the internal consistency of this hypothesis: i.e., if the premise of differences in physiological temperature sensitivities is granted, does the conclusion of tipping-point behavior follow? (Note that this question is different from asking whether Arctic marine ecosystems are likely to show tipping-point behavior in general, a question larger than any specific mathematical model.) We will show that over the range of conditions experienced in the EBS, and projected to be experienced there over coming decades, direct physiological responses to temperature in fact have only minor consequences compared with environmental correlates of temperature that modulate the light and nutrient environment for phytoplankton.

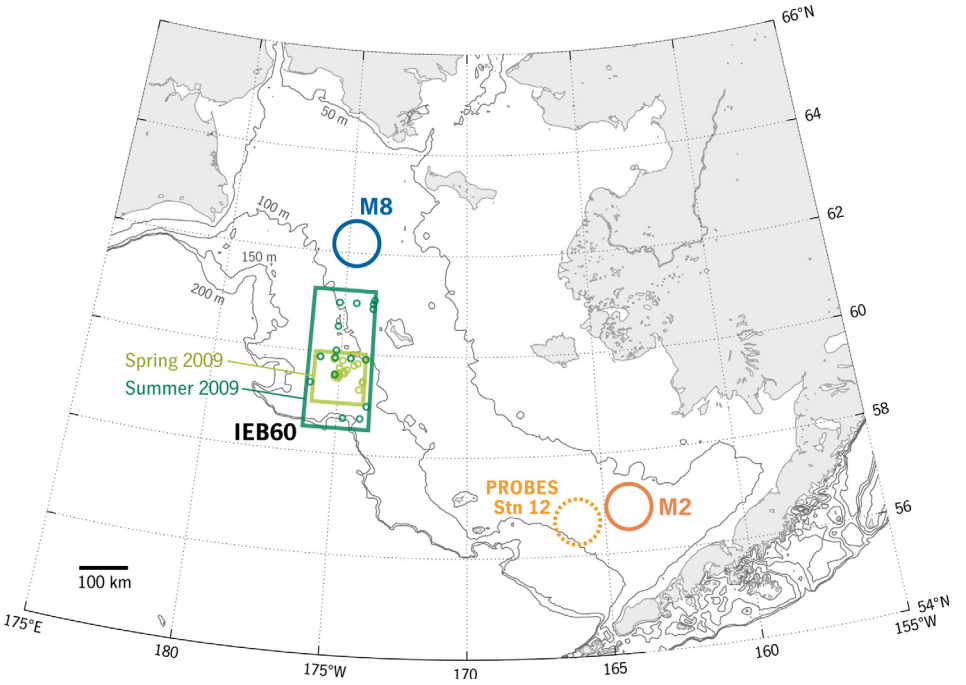

Figure 3. Study area and sites of model-data comparisons. Long-term mooring sites M2 and M8 [*Stabeno et al*., 2012a], along with PROBES Station 12 [*Sambrotto et al*., 1986], are marked with 50 km radius circles, the area over which model time series were extracted from particle-path ensembles. The bounds for CTD matchups with the "IEB60" model experiment (see text) are marked by light and dark green rectangles for spring and summer 2009, with individual CTD stations marked by small circles. The 50, 100, 150, and 200 m isobaths are also shown.

2. The Model

2.1. Physical Hindcast and Forecast

The BESTMAS (Bering Ecosystem Study ice-ocean Modeling and Assimilation System) model has been described and validated in detail by *Zhang et al*. [2010a] and Zhang et al. [2012]. The model domain covers the Northern Hemisphere north of 39°N, with highest horizontal resolution along the Alaskan coast and in the Eastern Bering Sea. Average grid spacing in the Bering Sea is 7 km, ranging from 2 km along the Alaskan coast to 12 km along the Aleutian Chain. Twenty-six ocean grid cells across Bering Strait allow a good connection between the Bering Sea and the Arctic Ocean.

The sea ice component of BESTMAS is an eight-category thickness and enthalpy distribution (TED) sea ice model [*Hibler*, 1980; *Zhang and Rothrock*, 2001] that employs a teardrop viscous-plastic rheology [*Zhang and Rothrock*, 2005], a mechanical redistribution function for ice ridging [*Thorndike et al*., 1975; *Hibler*, 1980], and a line successive relaxation (LSR) dynamics model to solve the ice momentum equation [*Zhang and Hibler*, 1997]. The TED ice model also includes a snow thickness distribution model following *Flato and Hibler* [1995]. It assimilates satellite ice concentration and SST data following *Lindsay and Zhang* [2006]. The ocean model is based on the Parallel Ocean Program (POP) developed at Los Alamos National Laboratory [*Smith et al*., 1992; *Dukowicz and Smith*, 1994], and incorporates forcing from eight tidal constituents. Open boundary conditions at 39°N are taken from a global ice-ocean modeling and assimilation system [*Zhang*, 2005].

Atmospheric forcing is taken from daily NCEP/NCAR Reanalysis data (National Centers for Environmental Prediction/National Center for Atmospheric Research: *Kalnay et al*. [1996]). Model forcing also includes freshwater river runoff into the Bering and Arctic seas. For the Bering Sea, monthly climatological runoffs of the Anadyr, Yukon, and Kuskokwim Rivers are used [*Zhang et al*., 2010a]. *Zhang et al*. [2010a] demonstrated that BESTMAS is able to capture much of the observed spatiotemporal variability of sea ice extent and thickness, the basic wind-forced and tide-forced features of upper ocean circulation, and seasonal and interannual variability of surface ocean temperatures at mooring site M2 (Figure 3).

This study uses daily output from a BESTMAS hindcast 1971–2012, similar to the period analyzed by *Zhang et al*. [2012]. It also uses a projection of conditions 2040–2050, which was created by randomly resampling

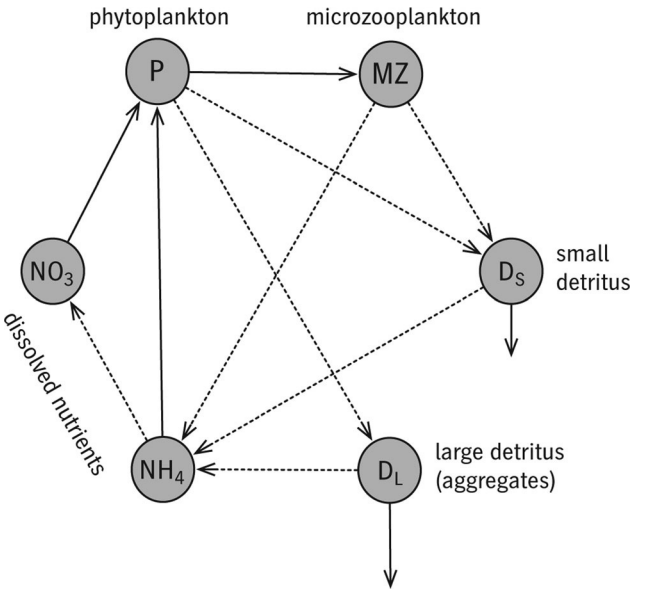

Figure 4. Structure of the ecosystem model. Solid arrows denote growth and dotted arrows denote regeneration pathways.

years from the hindcast and adding a linear temperature trend to the atmospheric forcing. The trend used is 8°C by 2100, close to the observed trend 1977–2012, and also close to the ensemble mean of IPCC global climate model projections for the Arctic Ocean [*IPCC*, 2007; *Wang et al*., 2012]. We will refer to this model projection as "the 2040s" for brevity, although of course if the course of future warming differs from the mean of current models, conditions like those depicted by this model run might arise sooner or later than the 2040s. Note that this approach does not attempt to resolve future change in mesoscale atmospheric patterns or storm frequency and intensity.

2.2. Ecosystem Model

The ecosystem model is a relatively simple, six-compartment nitrogen budget (Figure 4), which tracks NO_3, NH_4, phytoplankton biomass P, microzooplankton biomass Z, and small and large detritus D_S, D_L. This model structure is a simplification of an initial model version containing two phytoplankton classes, microzooplankton, stage-resolved copepods, and euphausiids. Extensive experiments varying both the structure and parameter values in this model ($\sim$200,000 cases) led to the conclusion that the added complexity offered no improvement in performance against the phytoplankton/microzooplankton observations shown below (section 3). This finding is consistent with the more formal investigation of model complexity by *Ward et al*. [2013]. Note also that in contrast to the microzooplankton, whose measured and modeled grazing rates are comparable to phytoplankton community growth rates, *Campbell et al*. [2016] determined mesozooplankton grazing to be $<$8% of primary production during bloom conditions, and so it is not surprising that the effect of omitting them from the model on both growth and export in spring falls within parameter uncertainty. (This might not be the case during summer or full-year simulations.)

The ecosystem model was not run fully coupled to BESTMAS in three dimensions, but rather in ensembles of one-dimensional, flow-following water-column environments. Time series of depth-resolved temperature T and vertical tracer diffusivity κ, along with photosynthetically available radiation PAR_0 at the water surface under ice, were extracted from BESTMAS following the trajectories of particles that track the 0–35 m depth-average currents. Particles were released 15 February of each model year, one per horizontal grid cell. These depth-versus-time fields form individual, noninteracting environments in which the ecosystem model is run. Each environment spans the entire water column with time-varying bottom depth, and has 15 vertical levels with resolution concentrated at the surface. Once initialized with a profile of nitrate concentration on 15 February, there are no exchanges through the sidewalls or bottom of each environment. This approach neglects horizontal gradients below the euphotic zone and nonlinear interactions between neighboring plankton communities, but the massive scale of the shelf system relative to typical near-surface currents [*Stabeno et al*., 2012b] and—crucially—the limited duration of our simulations (150 days) make the method appropriate, as it would not be for, say, yearlong simulations of a narrow shelf. This method offers huge gains in computational efficiency relative to a three-dimensional coupled model and therefore the opportunity to properly explore the model parameter space. The Lagrangian basis of the extracted physical forcing time series overcomes the worst of the limitations of one-dimensional Eulerian plankton models, which are in fact still widespread and useful tools [*Fasham et al*., 2006; *Bagniewski et al*., 2011], many others).

With one exception (the IEB60 ensemble described below), each of the ensembles used in this study was constructed as the set of particle trajectories that pass within 50 km of a given station at some

point within the simulation period (5). This hybrid Lagrangian/Eulerian method may appear roundabout compared with simply running a conventional, fixed-in-space, one-dimensional model at station, but it offers the crucial advantage of resolving (depth-averaged) lateral transport past each station, an ability which we will show is important to the interpretation of results at M2 (section 3.2). Each model simulation runs 15 February to 15 July of a given year, resolving the spring bloom and the transition into summer. This period was selected to match the seasonal coverage of BEST/BSIERP observations, 2007–2010.

Initial profiles of nitrate are constructed as an empirical function of water-column depth H alone:

$$\mathrm{NO}_3^{\mathrm{initial}}(z,H) = -\frac{z}{H}\mathrm{NO}_3^{\mathrm{bot}} + \left(1+\frac{z}{H}\right)\mathrm{NO}_3^{\mathrm{surf}} \tag{1a}$$

where

$$\mathrm{NO}_3^{\mathrm{bot}} = (42\ \mathrm{mmol\ m^{-3}})\frac{H^2}{(116\ \mathrm{m})^2+H^2} \tag{1b}$$

$$\mathrm{NO}_3^{\mathrm{surf}} = (24\ \mathrm{mmol\ m^{-3}})\frac{H^2}{(86\ \mathrm{m})^2+H^2} \tag{1c}$$

Values in (1b) and (1c) are based on Type III fits to bottle samples within 10 m of the bottom and 2 m of the surface, respectively, from spring 2009 BEST observations [*Mordy et al.*, 2012]. Because of the simplicity of this initial condition, interannual variation in over-winter replenishment of the nutrient pool is only partially resolved. A full treatment of this mechanism probably requires a fully coupled 3-D simulation.

The model equations are as follows:

$$\frac{dP}{dt} = q_P\mu(E,\mathrm{NO_3},\mathrm{NH_4})P - q_Z I(P)Z - q_R m_P P - q_P m_{agg}P^2 + \mathrm{mixing} \tag{2}$$

$$\frac{dZ}{dt} = \epsilon q_Z I(P)Z - q_Z m_Z Z^2 + \mathrm{mixing} \tag{3}$$

$$\frac{dD_S}{dt} = (1-\epsilon-f_{ex})q_Z I(P)Z + q_R m_P P - q_R r_{remin} D_S + \mathrm{sinking} + \mathrm{mixing} \tag{4}$$

$$\frac{dD_L}{dt} = q_P m_{agg}P^2 - q_R r_{remin} D_L + \mathrm{sinking} + \mathrm{mixing} \tag{5}$$

$$\frac{d\mathrm{NH_4}}{dt} = -f_\kappa \frac{\varphi_{\mathrm{NH4}}\mathrm{NH_4}}{N_{tot}} q_P\mu P + f_{ex}q_Z I(P)Z + q_R r_{remin}(D_S+D_L) - q_R r_{nitr}\mathrm{NH_4} + \mathrm{mixing} \tag{6}$$

$$\frac{d\mathrm{NO_3}}{dt} = -f_\kappa \frac{\mathrm{NO_3}}{N_{tot}} q_P\mu P + q_R r_{nitr}\mathrm{NH_4} + \mathrm{mixing} \tag{7}$$

See Table 1 for a summary of definitions and parameter values. Briefly, phytoplankton population growth is a balance among individual growth (the μ term), microzooplankton grazing, mortality, and aggregation; microzooplankton population growth is a balance between prey assimilation and mortality; and the detrital pools are controlled by a balance between these biological loss and uptake terms, remineralization, sinking, and nitrification. The factors q_P, q_Z, and q_R represent the temperature dependencies of phytoplankton metabolism, zooplankton metabolism, and respiration/bacterial metabolism respectively, each controlled by a Q_{10} factor, e.g.,

$$q_P \equiv Q_P^{T/10^\circ\mathrm{C}} \tag{8}$$

where T is temperature. The base model case uses a Q_{10} of 2 for phytoplankton growth and 2.8 [*Hansen et al.*, 1997] for processes mediated by bacteria and zooplankton. The implications of this and a spectrum of alternate choices are considered in section 3.4 below. Note that Q_Z is applied to both the growth/ingestion of the explicitly modeled microzooplankton and also the growth/ingestion of their implicit predators, i.e., microzooplankton mortality.

Table 1. Free Parameters of the Ecosystem Model[a]

Parameter	Symbol	Value	Units	Source
Phytoplankton				
Maximum *P* growth rate	μ_0	**1.2**	day^{-1}	Summer data [*Zeeman and Jensen*, 1990], temperature corrected
Light attenuation by seawater	att_{sw}	0.05	m^{-1}	
Light attenuation by phytoplankton	att_P	**0.006**	$m^{-1}\ \mu M\ N^{-1}$	1% light level and chl concentration, spring 2009 ice-free stations (E. Cokelet, personal communication, 2015)
Initial growth-light slope, winter	α_{win}	0.01	$(Wm^{-2})^{-1}d^{-1}$	
Initial growth-light slope, summer	α_{sum}	**0.16**	$(Wm^{-2})^{-1}d^{-1}$	*Sambrotto et al.* [1986], bloom maximum
Light level of $\alpha_{win}/\alpha_{sum}$ transition	E_{crit}	30	Wm^{-2}	
Width of $\alpha_{win}/\alpha_{sum}$ transition	ΔE	5	Wm^{-2}	
Minimum half-saturation for NO_3	k_{min}	0.16	μM N	*Collos et al.* [2005]
Preference for NH_4	φ_{NH4}	2		
Phytoplankton C:N ratio		**9**	mol:mol	Spring 2009 observations [*Sambrotto et al.*, 2016]
Chlorophyll:N ratio		**2.2**	mg:μM	C : chl=50 at bloom stations
Phytoplankton mortality	m_P	0.03	day^{-1}	
Phytoplankton loss via aggregation	m_{agg}	0.009	$(\mu M\ N)^{-1}\ d^{-1}$	
Zooplankton				
Max microzooplankton ingestion rate	I_0	**3.4**	day^{-1}	Dilution experiments, spring 2009 [*Sherr et al.*, 2013]
Grazing half-saturation	K	1	μM N	*Sherr and Sherr* [2009]
Microzooplankton growth efficiency	ϵ	0.3		*Hansen et al.* [1997]
Fraction of grazing excreted to NH_4	f_{ex}	0.35		
Microzooplankton mortality	m_Z	1.5	day^{-1}	
Regeneration and Export				
Small detritus sinking rate	w_S	3	$m\ d^{-1}$	
Large detritus sinking rate	w_L	100	$m\ d^{-1}$	
Detrital remineralization rate	r_{remin}	0.05	day^{-1}	
Nitrification rate	r_{nitr}	0.03	day^{-1}	cf. *Zhang et al.* [2010b]
Temperature Dependence				
Q_{10} for phytoplankton	Q_P	2		*Bissinger et al.* [2008]
Q_{10} for zooplankton	Q_Z	2.8		*Hansen et al.* [1997]
Q_{10} for bacterial respiration	Q_R	2.8		
Initial Conditions				
Integrated phytoplankon	P	**6**	μM N m	prebloom chlorophyll, spring 2009 [*Lomas et al.*, 2012]
Integrated microzooplankton	Z	**0.4**	μM N m	prebloom C biomass, spring 2009 [*Sherr et al.*, 2013]
Small detritus	D_S	0		
Large detritus	D_L	0		
Nitrate	NO_3	equation (1)		*Mordy et al.* [2012]
Ammonium	NH_4	0		

[a] μM N ≡ mmol nitrogen m^{-3}. All rates are reported at 0°C. Parameter values calculated from local data are in bold.

2.3. Phytoplankton Growth

Individual phytoplankton growth and nutrient uptake are considered equivalent in this model, as in many NPZ-style models. Specific growth rate μ depends on light and nutrients as

$$\mu = \left(\frac{\alpha E}{\sqrt{\alpha^2 E^2 + \mu_0^2}}\right)\left(\frac{N_{tot}}{k_{min} + 2\sqrt{k_{min} N_{tot}} + N_{tot}}\right)\mu_0 \tag{9}$$

The maximal rate μ_0 was based on summer observations by *Zeeman and Jensen* [1990], temperature corrected using a Q_{10} of 2 and a seasonal temperature difference of 7°C. Nutrient limitation follows the optimal-uptake scheme of *Smith et al.* [2009] in which, consistent with global observations [*Collos et al.*, 2005], the effective half-saturation $k_{min} + 2\sqrt{k_{min} N_{tot}}$ increases with nutrient concentration from a minimum value k_{min}, based on an optimization of intracellular resources for cell-surface uptake and internal transport. $N_{tot} = NO_3 + \varphi_{NH4} NH_4$ is effective total nutrient concentration, where φ_{NH4} is a preference for NH_4 defined by analogy with a common formulation of grazing on multiple prey types [*Gentleman et al.*, 2003].

Photosynthetically available radiation (PAR) at a given depth, $E(z)$, is attenuated from BESTMAS-derived surface PAR E_0 (0.43 shortwave radiation) by both seawater and overlying phytoplankton:

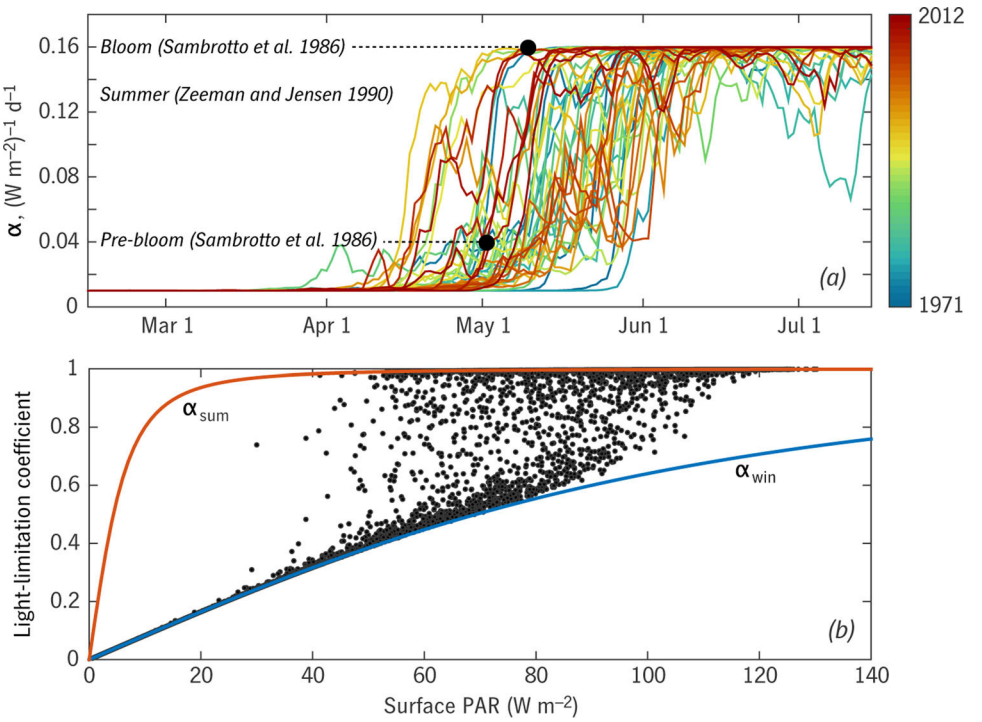

Figure 5. (a) Modeled time histories of α according to equation (11) for each hindcast year at mooring M2. Black dots show the two values measured at PROBES Station 12 (see Figure 3) in 1981 [*Sambrotto et al*., 1986, Figure 14]. The rate of increase between these two values is consistent with the range of rates of increase that arise in the model. (b) Black dots give daily values of the surface light-limitation coefficient $\alpha E_0(\mu_0^2+\alpha^2 E_0^2)^{-1}$ (see (9)) as a function of surface PAR E_0, across all hindcast years at M2. The upper and lower bounds on this functional response, corresponding to $\alpha=\alpha_{sum}$ and $\alpha=\alpha_{win}$ respectively, are shown as red and blue lines. Scatter in the functional response arises from the dependence of α on turbulent mixing in addition to E_0.

$$E(z)=E_0\int_z^{\text{surface}}(\text{att}_{sw}+\text{att}_P P(z))\,dz \tag{10}$$

In contrast to most simple NPZ models, the initial slope of the growth-light curve α is not fixed but rather varies seasonally. This behavior is based on observations by *Sambrotto et al*. [1986], who found that α increased more than fourfold over 8 days in the lead-up to the spring bloom in the southeastern Bering Sea in 1981 (Figure 5). Over these 8 days, the mixed layer shoaled from >60 m to <20 m, suggesting a release from light limitation. For simplicity, we have ignored the simultaneous increase in μ_0 seen in those observations; allowing seasonal increase in either of these parameters would likely produce qualitatively similar model behavior, and varying both would be redundant. Either physiological shifts or community shifts might lead to this sort of variability in α. In general, shade-adapted phytoplankton show lower μ_0 (i.e., maximum photosynthetic rate) than high-light adapted communities [*Palmer et al*., 2011], and both ice cover and high levels of turbulent mixing in ice-free areas in winter/early spring would lead to shade adaptation [*Cianelli et al*., 2004; *Palmer et al*., 2011]. Note that these high-latitude observations run exactly contrary to the assumption of optimality-based models like *Pahlow and Oschlies* [2013] in which phytoplankton dynamically allocate their resources in order to maximize instantaneous growth rate.

In our model, α changes between a winter/prebloom value α_{win} and a spring bloom/summer value α_{sum}, in response to a light index E_{eff}:

$$\alpha=\alpha_{win}+\frac{1}{2}(\alpha_{sum}-\alpha_{win})\left(1+\tanh\frac{E_{eff}-E_{crit}}{\Delta E}\right) \tag{11}$$

E_{eff} uses a few essential scalings to represent light conditions as experienced by phytoplankton taking into account both surface light E_0 and turbulent diffusivity κ:

$$E_{eff} = E_0 \exp\left(-\mathrm{att}_{sw}\sqrt{\frac{\max \kappa}{\mu_0}}\right) \quad (12)$$

The square-root quantity is proportional to the depth over which a near-surface population is mixed in one doubling time. This formulation is inexact—appropriate as a scaling law only—but in the absence of a detailed physiological model of how the phytoplankton accomplish this change in α, and with the constants E_{crit} and ΔE determined by tuning, further detail was deemed to be unwarranted. This scheme for α produces rates of change in light sensitivity consistent with the observations by *Sambrotto et al*. [1986] (Figure 5a; slope of model curves in spring versus two observational values). A more specific rationale for this scheme over the alternatives is discussed in section 3.1.1.

2.4. Grazing, Losses, and Regeneration

Phytoplankton in the model are subject to both a constant linear mortality m_P representing viral lysis and predation by mesozooplankton, and also a density-dependent loss to the fast-sinking D_L pool representing aggregation of diatom blooms. The model performs distinctly better (with respect to *f*-ratio and *e*-ratio: section 3.1.1) with both of these loss terms included than it does with either alone.

A generally larger loss is explicit grazing by microzooplankton *Z*. The community grazing rate *g*, as measured by dilution experiments [*Sherr et al*., 2013; *Stoecker et al*., 2013a] is given by

$$gP \equiv q_Z I(P) Z \quad (13)$$

where $I(P)$ is the microzooplankton ingestion rate, here assumed to follow a simple saturating response:

$$I(P) = I_0 \frac{P}{K+P} \quad (14)$$

I_0 was determined empirically (3.4 ± 1.4 day^{-1}) by taking the mean of gP/Z (see 13) over seven dilution experiments from spring 2009 [*Sherr et al*., 2013] in which $P > 400$ mg C m^{-3}, i.e., $P \gg K$, with K estimated coarsely from the laboratory experiments reviewed by *Sherr and Sherr* [2009] as 1 mmol N m^{-3}. As did *Banas et al*. [2009], we credit the descriptive power of our very simple NPZ formulation (Figure 4) largely to the availability of a local, empirical constraint on microzooplankton grazing.

Microzooplankton mortality is quadratic. This form replicates the time-evolution of mesozooplankton predation as captured by an expanded version of the model with explicit, stage-resolved, *Calanus*-like copepods. Other predators whose production is timed differently relative to the spring bloom would lead to mortality on microzooplankton with a different functional form.

Slow-sinking and fast-sinking detrital pools export material from the surface layer. Estimates of overall *e*-ratio (vertical export as a fraction of primary production) by *Cross et al*. [2012] (0.29 ± 0.12 at 40 m depth for the seasonal range modeled here) were used to constrain the choice of D_S sinking rate w_s. The model proved to be insensitive to D_L sinking rate as long as the value is on the order of 10 m d^{-1} or higher. The detrital pools remineralize to NH_4 and NH_4 nitrifies back to NO_3 at relatively low rates compared with values commonly assumed in temperate plankton models, but similar to those used by *Zhang et al*. [2010b] in an Arctic model. This geographic variation is broadly consistent with the explicit temperature dependence Q_R assumed here.

2.5. Tuning and Validation Experiments

Two data sets were used for tuning and validation (Figure 3). First, we assembled a process-rich time series resolving an intense ice-edge spring bloom near 60°N in late April/early May 2009 from a variety of 2009 BEST/BSIERP observations [*Lomas et al*., 2012; *Mordy et al*., 2012; *Stabeno et al*., 2012b; *Stoecker et al*., 2013a; *Sherr et al*., 2013; *Sambrotto et al*., 2016]. Figure 3 shows an ensemble of 98 model particle trajectories that intersect the region where the bloom peak was sampled (174°W–176°W, 59°N–60°N) on 27 April 2009 during the spring BEST/BSIERP cruise. The trajectories diverge over the following months, and so observations over a larger area (173.75°W–176.25°W, 58.5°N–61.25°N) were selected from the summer cruise to represent the fate of the sampled bloom community. Time series of BESTMAS forcing along these 98 trajectories are shown in Figure 6 (note the temporary ice retreat in March 2009 described by *Miksis-Olds et al*. [2013]) and spring and summer cruise observations along with model results are shown in Figure 7. This observational data set ("IEB60") served as the primary standard for parameter tuning.

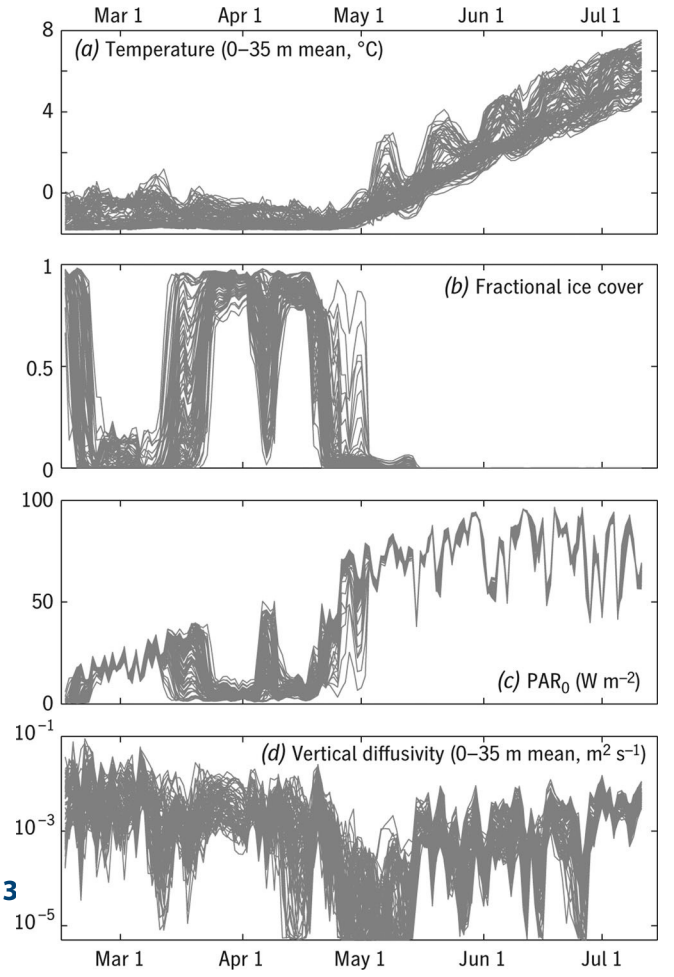

Figure 6. Forcing time series for the IEB60 ensemble (see Figures 3 and 7) extracted from BESTMAS.

Second, *Sigler et al*. [2014] report statistics describing bloom timing and other metrics at four long-term mooring stations along the 70 m isobath. We constructed model time series at M2 and M8, the northernmost and southernmost of these (Figures 3 and 8) and compared them with the *Sigler et al*. [2014] statistics. This served as a test of the spatial and temporal portability of the model, and also a basis for tuning E_{crit} and ΔE.

Values for att_{sw}, α_{win}, m_P, m_{agg}, m_Z, w_S, and r_{remin} were determined through a series of Monte Carlo experiments in which model runs using random combinations of parameters (n ≈ 100,000, alongside another 100,000 exploring structural variants) were compared with a suite of biomass, rate, and ecosystem-function metrics at IEB60. The same analysis was used to verify the appropriateness of a priori values for μ_0, att_P, att_{sum}, I_0, r_{nitr}, and biomass initial conditions. Sources for these and other parameter values are given in Table 1.

3.1. Model Validation

3.1.1. Evolution of an Ice-Edge Spring Bloom

The time course of the spring bloom at IEB60 is shown in Figure 7, and metrics of model performance are listed in Table 2. Nitrate in the upper 35 m declined precipitously as phytoplankton biomass increased to very high levels (Figures 7a and 7b). Observations of nitrate around 27 April shown great variability (0–15 mmol m^{-3}) but this appears to be explicable by variation in ice cover and light within this 100 km region (Figure 6, spread in model ensemble). Error in nitrate in July (Figure 7a) is probably a combination of errors in vertical structure near the pycnocline—some of the high observational values represent pycnoclines shallower than 35 m, rather than cross-pycnocline fluxes—but also a failure of our model to reproduce the intermittent resupply of nitrate to the surface layer via patchy wind mixing. This may reflect the limits of our Lagrangian ensemble approach compared with a full three-dimensional biogeochemical simulation.

The model captures the timing of the spring bloom within a few days (Figure 7b). Data in this region of the shelf from other BEST field years [*Sambrotto et al*., 2016] confirm the approximately 20 day spin-up time of the bloom. Peak integrated biomass (measured by two independent data sets: *Lomas et al*. [2012] and *Sambrotto et al*. [2016]) is biased low in the model by 21% even after extensive tuning, because error in this metric is involved in a strong tradeoff with errors in *e*-ratio and prebloom biomass. Bias in summer phytoplankton biomass is smaller in absolute terms but higher in relative terms; we did not weight this time period as strongly in the parameter-tuning process.

Note that the model value for light attenuation by phytoplankton att_P was chosen based on a detailed, unpublished calculation of 1% light level at spring 2009 BEST stations in relation to chlorophyll concentration (E. Cokelet, personal communication, 2015). The value used for att_{sw} is an ad hoc downward adjustment of the estimate from that analysis (from approximately 0.1 to 0.05 m^{-1}). This adjustment proved to be necessary

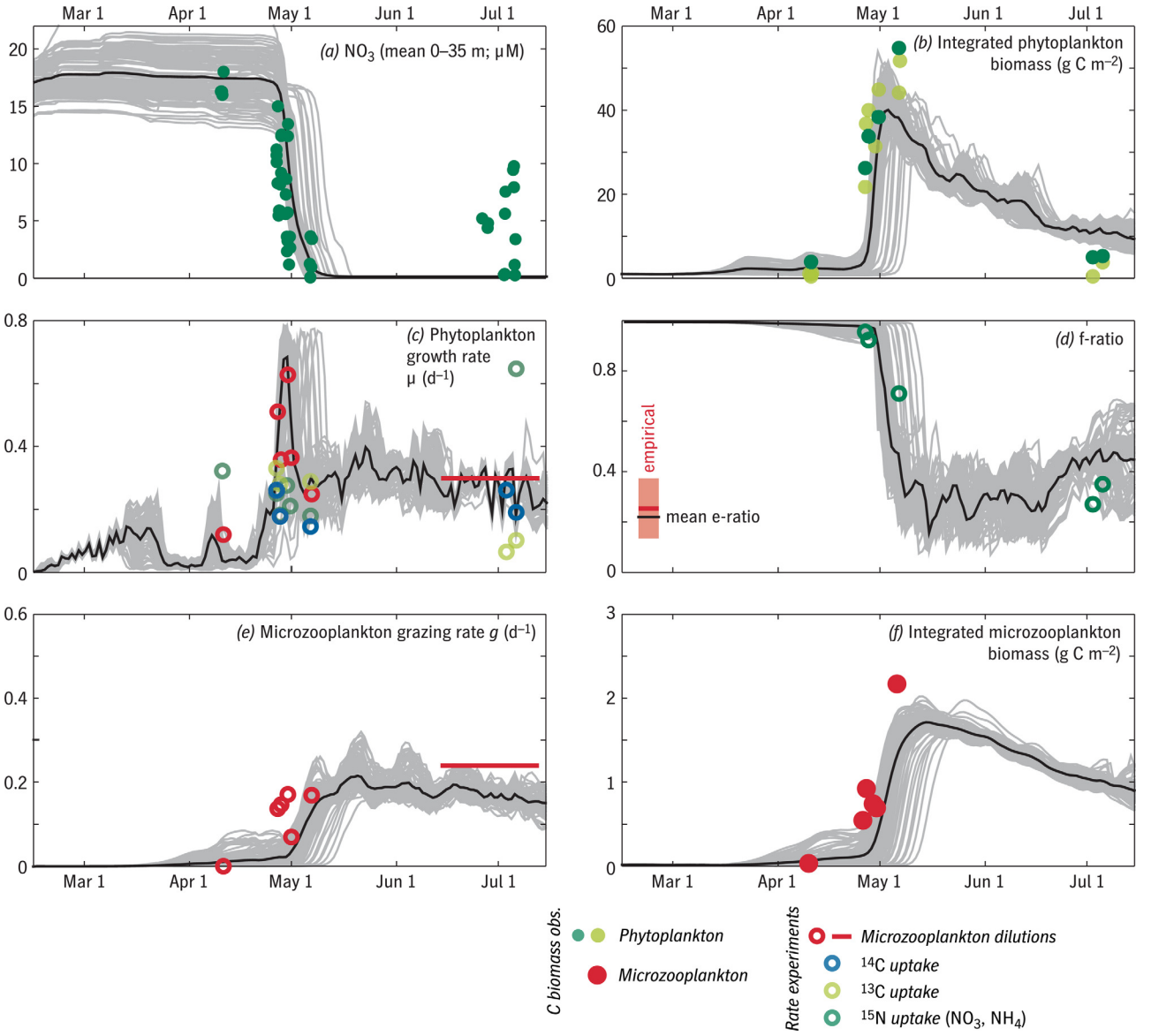

Figure 7. Time history of an ice-edge bloom in spring 2009 from observations and the model. Individual model cases—responses to the 98 individual forcing trajectories in the IEB60 ensemble (Figures 3 and 6)—are shown as gray lines, and the ensemble mean as a black line. Solid circles denote standing-stock measurements (nitrate and phytoplankton: light and dark green; microzooplankton: red), while open circles denote rate measurements (microzooplankton dilution experiments: red; ^{14}C, ^{13}C, ^{15}N uptake experiments: blue, light green, dark green). Red bars in Figures 7c and 7e denote areal means from *Stoecker et al.* [2013a] (north/mid-north, middle/outer, in that study) over the duration of the summer 2009 cruise. An empirical estimate of mean export ratio ±1 std dev (red) is shown along with the model value in Figure 7d (inset). Data sources are discussed in the text.

to capture the magnitude of the IEB60 bloom without distortions in other metrics. We speculate that this artificial reduction in light attenuation compensates for bias in the vertical structure of turbulent mixing either in BESTMAS or in our one-dimensional reimplementation. At IEB60, our ad hoc adjustment in att_{sw} is equivalent to a change of 0.15 day^{-1} in mean growth rate over the euphotic zone, enough to cause a twofold change in biomass accumulation over 5 days. It would only take a bias of 4 m in the depth over which euphotic-zone phytoplankton are mixed in the model—a bias smaller than our vertical resolution—to have a comparable effect on growth rate. These extreme sensitivities suggest that beyond a factor of 2 or so, it would be unwarranted to place special emphasis on any model's skill at reproducing absolute chlorophyll concentration in this region, compared with other timing or functional metrics.

The model reproduces observed rates and rate ratios at IEB60 well. Four independent observational estimates of phytoplankton community growth rate, from microzooplankton dilution experiments and ^{14}C, ^{13}C, and ^{15}N uptake experiments, are shown in (Figure 7c). The model ensemble-average time series of μ (Figure

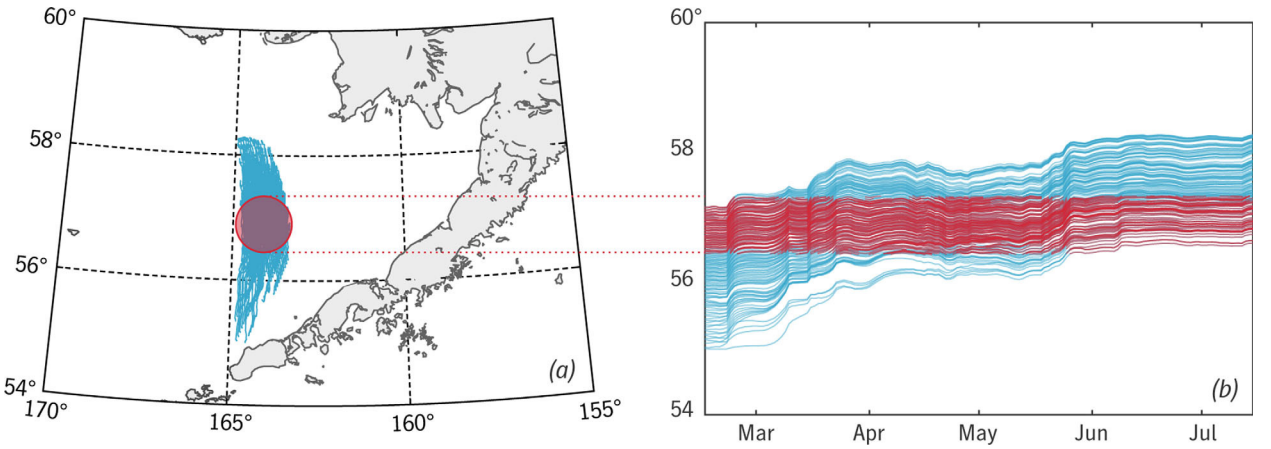

Figure 8. Example of an ensemble of surface-layer particle trajectories used as the environment for a seasonal model run. (a) Blue lines indicate particles passing within 50 km of mooring station M2 (red circle) at some point within the 15 February to 15 July model run in 2002 (an example year). (b) The same particle paths, plotted as latitude versus time; each continuous line represents a distinct ecosystem model run. The segments of these trajectories $<$ 50 km from M2 are shown in red. Final model time series at M2 were constructed by averaging across the highlighted segments.

7c) matches the observations as well as well the four observational time series match each other, following the dilution experiment data (red) most closely. In spring (but not in summer), the model ensemble actually replicates the severalfold near-instantaneous variance of the observations, suggesting that this variance could be the result of physically forced, $<$100 km scale variation in bloom evolution.

The ratio of new, nitrate driven to total primary production (*f*) was estimated from the ratio of NO_3 to NH_4 uptake (Figure 7d) [*Sambrotto et al.*, 2016]. The *f*-ratio decreased from $\sim$1 at the height of the bloom to $\sim$0.3 in July (Figure 7d), and the model—despite inclusion of only one phytoplankton compartment—replicated this shift. The mean *e*-ratio for the spring-summer analysis period is also shown in Figure 7d, as estimated by *Cross et al.* [2012] for the middle-outer shelf as a whole and for the model at IEB60, where the modeled value falls within the range of empirical uncertainty.

Table 2. Detailed Metrics of Model Performance at IEB60, Spring-Summer 2009[a]

Variable	Time Period	Obs. Value	Model Value
NO_3, 0–35 m (μM N)	10–11 Apr (prebloom)	16.5	17.4
	26–30 Apr (early bloom)	7.7	15.0
	6–7 May (late bloom)	1.9	1.6
	26 Jun to 6 Jul (summer)	4.3	0
Integrated phytoplankton ($g\ C\ m^{-2}$)	10–11 Apr	0.86	1.7
	26–30 Apr	34	10
	6–7 May	47	37
	26 Jun to 6 Jul	2.0	11
Integrated microzooplankton ($g\ C\ m^{-2}$)	10–11 Apr	0.0028	0.0055
	26–30 Apr	0.066	0.016
	6–7 May	0.18	0.11
Phytoplankton specific growth rate (day^{-1})	10–11 Apr	0.091	0.024
	26–30 Apr	0.38	0.41
	6–7 May	0.19	0.24
	26 Jun to 6 Jul	0.22	0.21
Specific grazing rate (day^{-1})	10–11 Apr	0	0.0076
	26–30 Apr	0.15	0.019
	6–7 May	0.17	0.12
	26 Jun to 6 Jul	0.24	0.17
f-ratio	26–30 Apr	0.94	0.99
	6–7 May	0.71	0.50
	26 Jun to 6 Jul	0.31	0.46
e-ratio	15 Feb to 15 Jul	$\sim$0.29	0.26

[a]Sources: *Mordy et al.* [2012], *Lomas et al.* [2012], *Cross et al.* [2012], *Sherr et al.* [2013], *Stoecker et al.* [2013a], and *Sambrotto et al.* [2016].

Finally, the model also captures microzooplankton biomass and grazing rate during the bloom (Figures 7e and 7f). Summer observations of microzooplankton biomass [*Stoecker et al*., 2013b] were not sufficiently resolved in the vertical to estimate in situ integrated biomass with confidence, and thus are not included. Only one of the July dilution experiments described by *Stoecker et al*. [2013a] fell within the narrow matchup region for the IEB60 ensemble and so the absolute in situ grazing rate is not as well constrained in summer, but the ratio g/μ for the ensemble in July is consistent with the observed ratio of rates for broader spatial averages in the *Stoecker et al*. [2013a] data set (Figures 7c and 7e).

Over the course of these observations at IEB60, the $>5\mu$m fraction of phytoplankton biomass changes significantly, from $\sim$0.5 before the bloom to $\sim$1 during the bloom to $\sim$0.2 in July (not shown). This data set is thus a complex test of a simple, 1-P NPZ model like ours, although it is parameterized to allow two modes of time variation in community functional responses (nutrient half-saturation and growth-light initial slope: see above) which can be taken in part to represent species composition shifts. As mentioned above, we ran extensive Monte Carlo experiments in a version of the model with a second phytoplankton compartment which was allowed its own nutrient and light responses, a distinct mortality rate, and a distinct susceptibility to microzooplankton grazing. We did not find any parameterization among these 2-P model cases that noticably outperformed the 1-P model version described here. Replicating the time evolution of the $>5\ \mu$m biomass fraction proved to be a major constraint on parameter combinations, but a constraint that was only weakly related to other skill criteria. At the same time, our Monte Carlo experiments clearly indicated that seasonal variation in α as described above was essential to reproducing the magnitude of ice-edge spring blooms while avoiding spurious late winter blooms. (Note that likely bias in the model light field is in the wrong direction to resolve the issue [*Ladd and Bond*, 2002], and that the earliest spring 2009 biomass and rate observations (Figure 7, below) are difficult to reconcile with any top-down explanation.)

3.1.2. Patterns of Bloom Timing

The diversity of simultaneous BEST/BSIERP observations allows us to verify the consistency of stocks, rates, and functional relationships during the IEB60 bloom event to a degree seldom possible with field data. A separate question, however, is whether the model, tuned to the IEB60 data set, is able to capture the diversity of spring bloom time histories across subregions and across years in the EBS. Figure 9a shows the relationship between ice-retreat timing t_{ice} (the date on which ice cover drops below 10%) and bloom timing t_{bloom} (the date of maximum integrated biomass) for all hindcast years at M2 and M8. The results replicate the essential pattern described by *Hunt et al*. [2002, 2011] and more recently quantified by *Brown and Arrigo* [2013] and Sigler et al. [2014] using satellite and moored observations, respectively. At M8, t_{ice} and t_{bloom} are close and well correlated, indicating an ice-retreat-triggered bloom in all years. At M2, the same association is seen in some years, but when t_{ice} is earlier than yearday 80, the spring bloom is delayed until May or early June. The model replicates this qualitative pattern (after tuning of E_{crit} and ΔE, but not other parameters, against the M2 data shown here). Year-by-year comparisons between observed and predicted t_{bloom} are quite good at M8 (Figure 9b), with a Willmott skill score of 0.86, where 1 represents a perfect model and 0 a model that performs no better than the mean of the observations [*Willmott*, 1981]. At M2 (Figure 9c), skill is significant (0.68) but errors of up to a month occur in some years. Comparisons of modeled and observed t_{bloom} at PROBES Station 12 [*Sambrotto et al*., 1986, Figure 3] are also shown in Figure 9c to extend the record.

Brown and Arrigo [2013] also report satellite-based t_{bloom} at M2 for nine ice-free years that overlap with the *Sigler et al*. [2014] moored observations. Remarkably, these two observational time series disagree with each other to the same extent as the model disagrees with either of them. Root-mean-square differences between model and mooring, model and satellite, and mooring and satellite are 16, 19, and 21 days, respectively (n = 9). Differences among the means are smaller (5, 1, and 4 days for the same three comparisons). This suggests that the date of maximum chlorophyll is an inherently noisy or ill-defined metric and that apparent signals with variance less than 2 weeks or so may not be significant.

3.2. Drivers of Interannual Variability

Full time series of modeled near-surface temperature, ice cover, and integrated phytoplankton and microzooplankton biomass at M8 and M2 are shown in Figures 10 and 11. Hindcast years have been resorted by mean temperature to better show relationships. A few patterns are evident by inspection: at M8, warm conditions are associated with earlier ice retreat, the timing of the spring bloom and ice retreat are closely

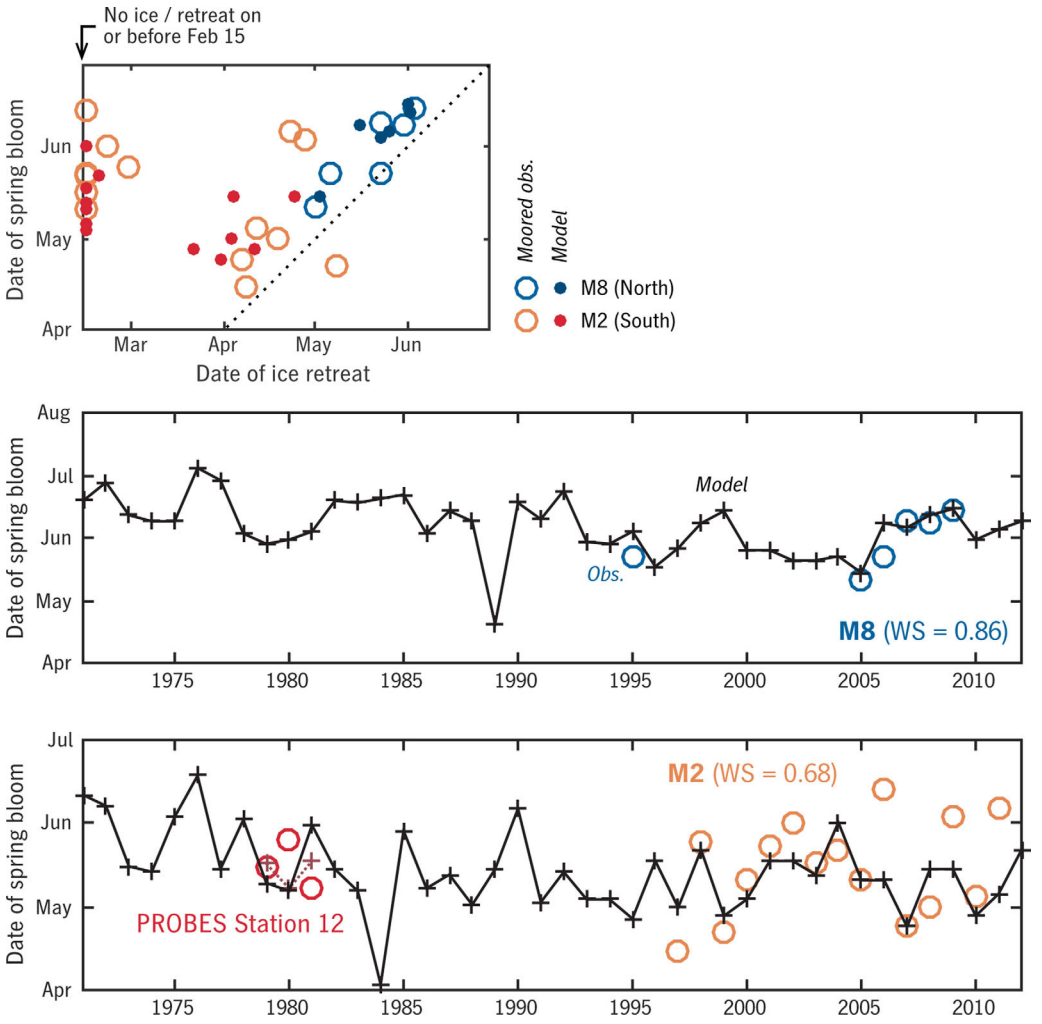

Figure 9. (a) Relationship between spring bloom timing and ice-retreat timing at M2 and M8 from observations [*Sigler et al.*, 2014] (open circles) and the model (solid dots). Years with no ice at M2 or ice retreat earlier than 15 February (the start of the NPZ simulation period) are plotted at 15 February, rather than omitted. (b and c) Date of the spring bloom maximum (as in Figures 9a and 9b) over time. Model time series are shown as lines, observations as open circles. Black line/crosses in Figure 9c show M2 results; for Probes Station 2, compare red circles (obs.) with red crosses (model).

associated, and microzooplankton biomass follows phytoplankton biomass, although somewhat integrated and smoothed. At M2, spring bloom timing follows ice-retreat timing in the minority of years when ice is present, but does not show a monotonic relationship with mean temperature overall. Modeled phytoplankton blooms at M2 are intermittent, with multiple peaks in most years, as seen in moored fluorometer observations there [*Stabeno et al.*, 2012a]. This intermittency is likely to contribute to the noisiness of the date of maximum chlorophyll as a timing metric.

There are a large number of confounded correlations among variables in these results, which complicate their mechanistic interpretation. In this section, we use a systematic correlation analysis and some ancillary model experiments to determine which relationships between environmental conditions and phytoplankton responses are actually causal in our modeled northern and southern EBS.

Modeled primary production is positively correlated with temperature at both M2 and M8 (Table 3 and Figure 12). Either direct effects or indirect correlates of temperature could be responsible, however. By "direct effects," we mean the appearances of temperature within the ecosystem model equations: these include direct physiological effects (like the Q_{10} dependence of phytoplankton maximum growth rate) and community-metabolism effects (like the imposed difference in Q_{10} responses for phytoplankton and zooplankton). We will return to these community dynamics in more detail later, but for now the crucial result is

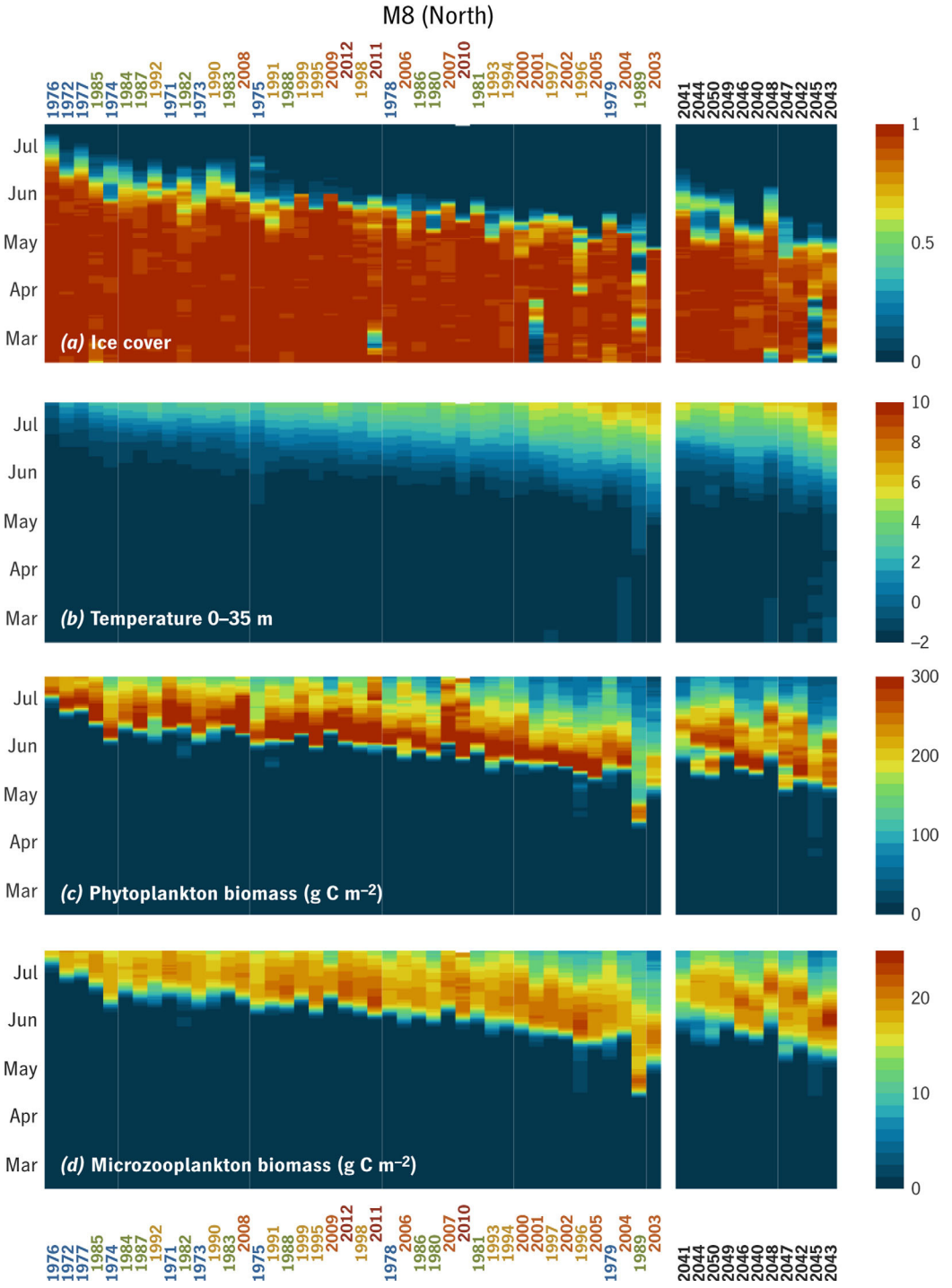

Figure 10. Model time series of (c and d) vertically integrated phytoplankton and microzooplankton biomass at M8 in relation to (a and b) temperature and fractional ice cover, for every year in the model hindcast and future projection. Years have been sorted by mean surface temperature within the hindcast and projection periods, in order to show patterns more clearly; individual years are labeled at top and bottom, color-coded, and staggered by decade.

that modeled primary production changes only marginally when we turn off all these direct temperature effects entirely. Figure 13 shows a comparison between mean 15 February to 15 July integrated primary production at M2 and M8 in the model base case and in a variant in which we set $Q_P = Q_Z = Q_R = 1$, so that all biological rates maintain their 0°C base value across all conditions. Results at M8 are essentially indistinguishable,

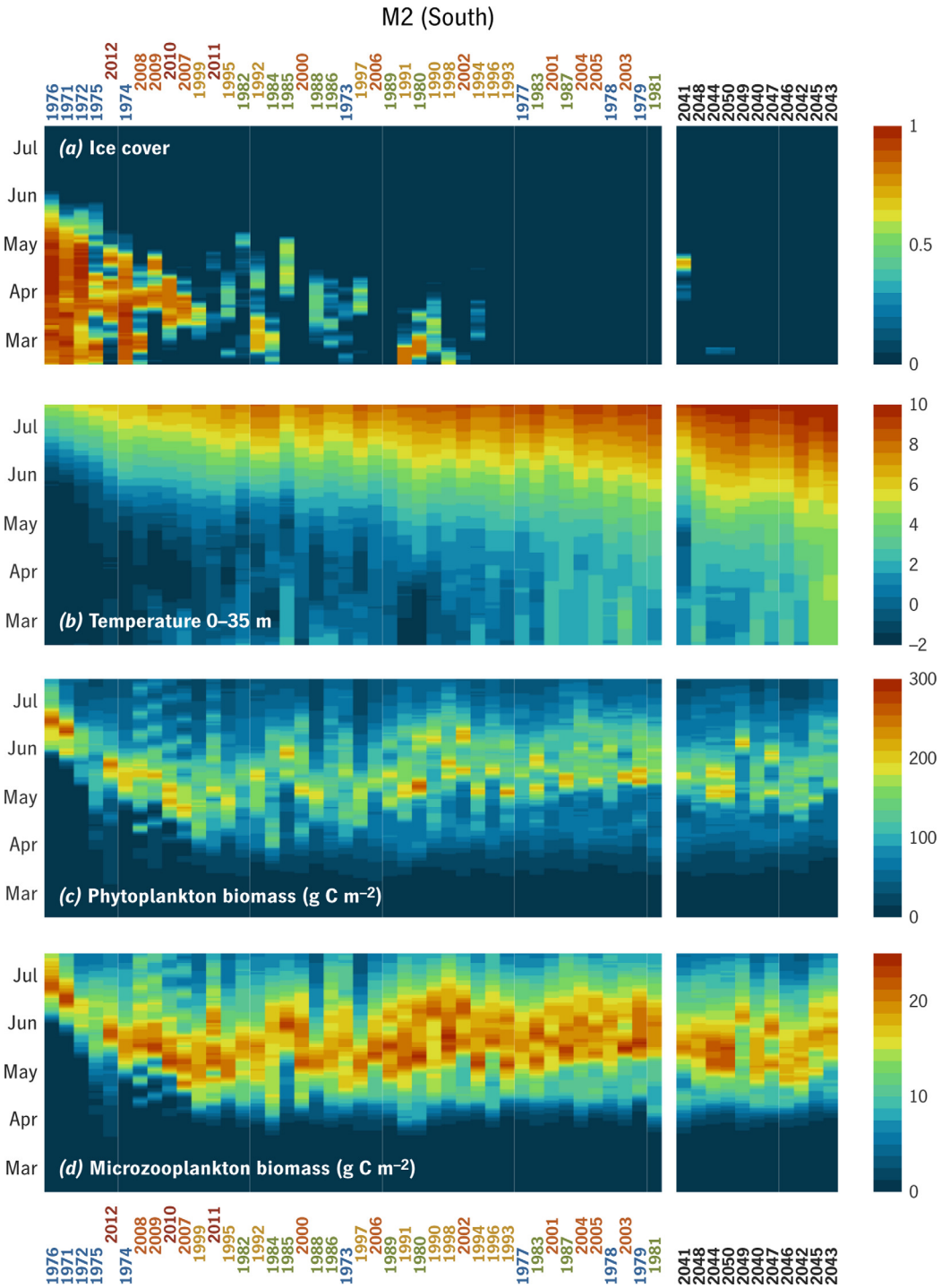

Figure 11. Time series for all years in the model hindcast and projection, as in Figure 10, for station M2.

and at M2 show a simple, close-to-linear bias. As one would expect, results from an intermediate case in which $Q_P = Q_Z = Q_R = 2$ (the Q_P base value) fall in between the case shown in Figure 13 and the 1:1 line.

The implication is that direct effects of temperature play only a small role in determining which model years have higher primary production than others. Results for t_{bloom} (not shown) are noisier but likewise indicate no overall causal role on the interannual scale we are considering. Among the correlates of temperature, then,

Table 3. Coefficients of Determination r^2 Between Forcing and Phytoplankton-Response Variables Across Model Hindcast Years, 1971–2012[a]

	$\overline{T_{35}}$	$\overline{ice}$	t_{ice}	$\overline{E_0}$	$\overline{E_{eff}}$	$\bar{\kappa}$	$\overline{u_{rot}}$
t_{bloom}, M8 (North)	0.82	0.88	0.83	0.90	0.79		
$\overline{PP}$, M8 (North)	0.43	0.55	0.58	0.65	0.60		0.26
t_{bloom}, M2 (South)				0.30	0.52		
$\overline{PP}$, M2 (South)	0.64	0.53	0.48	0.47		0.46	0.54

[a]Only correlations significant at the 0.1% confidence level are shown. Forcing variables included are 0–35 m mean temperature $\overline{T_{35}}$ (°C), mean fractional ice cover $\overline{ice}$, date of ice retreat t_{ice} (yearday), mean PAR at the water surface $\overline{E_0}$ (W m^{-2}), mean light index $\overline{E_{eff}}$ (W m^{-2}; see equation (12)), mean 0–35 m turbulent diffusivity $\bar{\kappa}$ (m^{-2} s^{-1}), and mean along-shelf transport $\overline{u_{rot}}$ (km d^{-1}). Response variables are date of spring bloom maximum t_{bloom} and mean integrated primary production $\overline{PP}$ (g C m^{-2} d^{-1}). All means are taken over the entire simulation period, 15 February to 15 July, except $\bar{\kappa}$, which is taken 1 April to 15 July.

which are most directly responsible for interannual variation in bloom timing and mean spring primary production (hereafter $\overline{PP}$) in the north and the south?

1. t_{bloom} at M8: mean spring fractional ice cover $\overline{ice}$, mean PAR at the water surface (under-ice when ice is present) $\overline{E_0}$, and the mean of the composite light index defined above $\overline{E_{eff}}$ are all well correlated with t_{bloom} (Figure 12 and Table 3) and with each other (Table 4). The most straightforward interpretation is that ice cover controls light availability and thereby the timing of the bloom.
2. t_{bloom} at M2: in the south, however, neither surface light availability ($\overline{ice}$, $\overline{E_0}$) nor turbulent mixing ($\bar{\kappa}$, the 0–35 m, 1 April to 15 July turbulent diffusivity) is well correlated with t_{bloom} by itself, but the composite light index $\overline{E_{eff}}$, which combines these surface and subsurface effects on light availability, is a moderately good predictor ($r^2 = 0.52$: Table 3). This is consistent with the classic picture (see section 3.1.2) in which ice retreat controls bloom timing at M2 in some years while early spring storms delay the bloom in others.
3. $\overline{PP}$ at M8: primary production in the north is correlated with the same factors as t_{bloom}, and inversely with t_{bloom}, implying that interannual variation in $\overline{PP}$ mainly reflects the position of the bloom within the 15 February to 15 July analysis window (see Figure 10).
4. $\overline{PP}$ at M2: here the correlation with t_{bloom} is weakly positive, indicating different dynamics. $\overline{PP}$ is correlated with $\overline{ice}$ and $\overline{E_0}$ overall (Figure 12) but these relationships fail to explain twofold variation in $\overline{PP}$ among ice-free years. The best correlate of $\overline{PP}$ at M2 is mean temperature, but this is necessarily an indirect relationship, as discussed above. The next best correlate is mean along-shelf transport $\overline{u_{rot}}$, calculated from the net motion 15 February to 15 July of particle trajectories that intersect M2 (see Figure 8). The component of net displacement oriented 120° was taken as along-shelf transport. (In our Lagrangian model setup, this metric indicates the water depth of the starting positions of each year's ensemble of

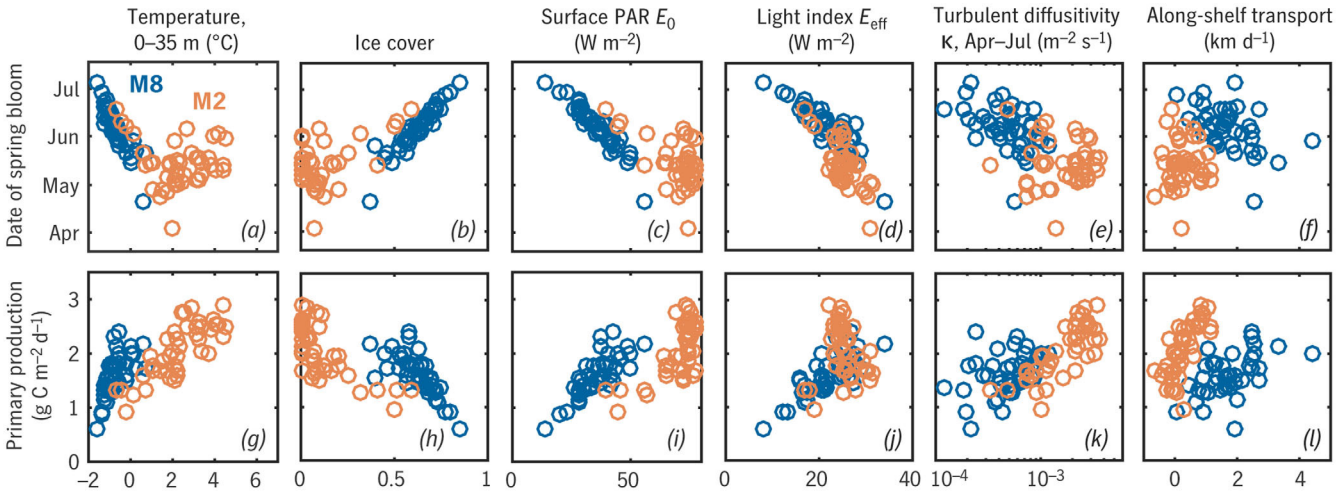

Figure 12. Relationships between six environmental forcing metrics and two metrics of the phytoplankton response, at M2 (orange) and M8 (blue). Each symbol represents one model hindcast year, averaged 15 February to 15 July except as otherwise noted. Cf. Table 3.

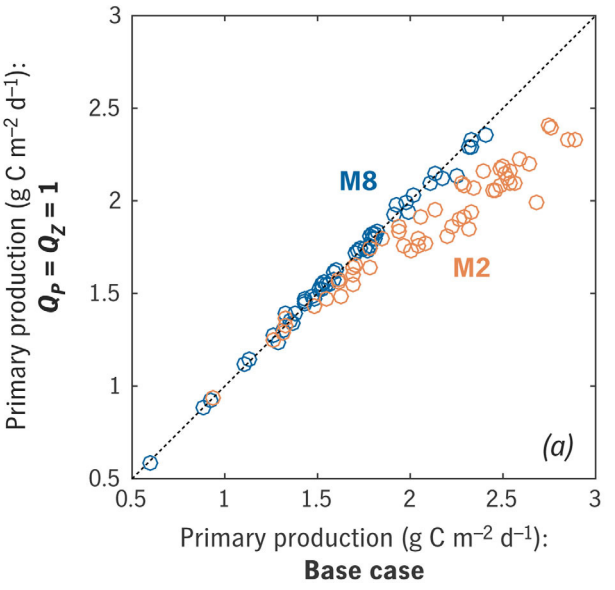

Figure 13. Comparison between mean primary production in the model base case and an alternate parameterization with direct effects of temperature omitted ($Q_P = Q_Z = Q_R = 1$), across hindcast years.

one-dimensional cases, and thus the nitrate initial condition (equation (1).) Since we are analyzing results as Eulerian time series extracted from the Lagrangian ensemble (Figure 8), $\overline{u_{rot}}$ can also be interpreted in a conventional way as the strength of advection of deep water nutrients past the station.) The residuals between $\overline{PP}$ and $\overline{u_{rot}}$ at M2 (not shown) are in turn correlated with $\bar{\kappa}$. This correlation is positive, suggesting the effect of turbulence on nutrient supply, not light limitation as above. Consistent with this interpretation, the slope between interannual variations in $\overline{PP}$ and $NO_3^{initial}$, relative to their 1971–2012 means, is steeper than 1:1 (Figure 14), whereas ancillary model experiments in which we manipulated $NO_3^{initial}$ directly (varying the leading coefficients in (1c) and (1b) by ±30%) show an almost exactly 1:1 relationship (Figure 14). This suggests that multiple mechanisms of interannual variation in nutrient supply—one lateral, one vertical—are at work simultaneously at M2, both of them correlated with seasonal-mean temperature.

3.3. Implications for Future Change

The importance of distinguishing causal from merely correlated environmental drivers becomes clear when we switch our focus to longer-term change in the model. Figure 15 shows t_{bloom} and $\overline{PP}$ at M2 in relation to a subset of the drivers shown in Figure 12. Here the 1971–1976 cold period is distinguished from the generally warmer period that followed (1977–2012: see Figure 1) and from the 2040s projection discussed above. The relationships that we identified above as causal remain consistent across the full model run, whereas relationships that we identified as indirect do not (most dramatically, compare Figures 15a and 15b). In this model run, the mean difference in bloom timing between warm and cold years described by the original Oscillating Control Hypothesis [*Hunt et al.*, 2002])—later blooms in warmer years—appears to be contingent on a particular decadal-scale regime, and does not continue to hold farther into either the past or the future. (Predictions based on ice cover rather than temperature are more consistent: not shown.)

Table 4. Coefficients of Determination r^2 Among Forcing Variables Across Model Hindcast Years, 1971–2012[a]

	$\overline{ice}$	t_{ice}	$\overline{E_0}$	$\overline{E_{eff}}$	$\bar{\kappa}$	$\overline{u_{rot}}$
M8 (North)						
$\overline{T_{35}}$	0.81	0.83	0.80	0.61		0.34
$\overline{ice}$		0.87	0.92	0.74		
t_{ice}			0.93	0.75		0.26
$\overline{E_0}$				0.86		
$\overline{E_{eff}}$						
$\bar{\kappa}$						
M2 (South)						
$\overline{T_{35}}$	0.73	0.67	0.65		0.68	0.28
$\overline{ice}$		0.80	0.95		0.47	
t_{ice}			0.73		0.52	
$\overline{E_0}$				0.25	0.32	
$\overline{E_{eff}}$						
$\bar{\kappa}$						0.34

[a]Only correlations significant at the 0.1% confidence level are shown. Variables are defined as in Table 3.

Likewise, 2040s $\overline{PP}$ in this model projection falls well below an extrapolation based on regression to temperature across the model hindcast years (bias of 0.5 g C m^{-2} d^{-1}, comparable to the mean difference in this model between warm and cold years of the 2000s). Relationships with $\overline{E_{eff}}$ and $\bar{\kappa}$ suggest why: these proximate controls on light and nutrient limitation are similar across the model hindcast and projection, even as seasonal-mean temperature changes by >2°C. This result is as likely to be a

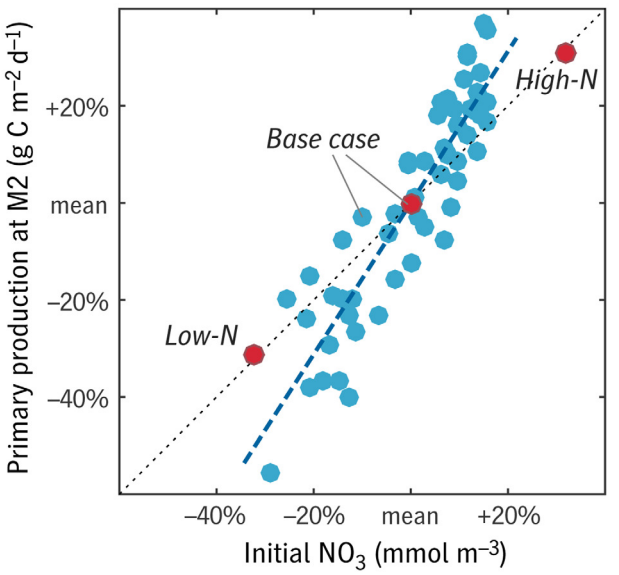

Figure 14. (blue) Relationship between initial NO_3 concentration (vertical mean and mean across ensemble members) and 15 February to 15 July mean primary production across model hindcast years at M2. (red) Comparison between model base case (mean of hindcast years/blue symbols) and two alternate model cases in which initial NO_3 was adjusted upward and downward by 30%. Values are shown as percent change relative to model base-case mean.

methodological artifact as a proper prediction, since the model projection used here is driven by a trend in the regional thermodynamics but not trends in the mesoscale dynamics that control seasonal flushing and storm mixing. Given the diagnosis of environmental drivers based on the model hindcast, there is no reason to think that we can extrapolate future change in t_{bloom} or $\overline{PP}$ in the southern, increasingly ice-free EBS from gross measures of surface temperature and ice cover (Figure 2). This cautionary result appears to be true for either statistical or dynamical extrapolations.

3.4. Trophic Coupling in Spring

Some researchers have suggested that in high-latitude systems, the degree of coupling between primary and secondary zooplankton production is highly temperature dependent and that this dependence is a major factor in structuring those ecosystems. *Rose and Caron* [2007], for example, suggest that microzooplankton grazing is limited by low temperatures to the point that it cannot keep up with phytoplankton growth at near-freezing temperatures, and that this partial decoupling is a major driver of the intense algal blooms often seen at high latitudes. Our model—or rather, the measured community growth and grazing rates at ~0°C that the model is based on [*Sherr et al.*, 2013]—is inconsistent with this hypothesized mechanism, and thus consistent with *Sherr and Sherr* [2009] and Franzè and Lavrentyev [2014]. When we compare time histories of microzooplankton and phytoplankton biomass at M2 and M8 (Figure 16a), we do see a greater time lag between the phytoplankton and their grazers at the colder site (phase-space trajectories more elliptical at M8, more linear at M2). Superficially this seems to corroborate the *Rose and Caron* [2007] hypothesis of a greater decoupling in colder conditions, but when we turn off direct temperature effects in the model ($Q_P = Q_Z = Q_R = 1$), the pattern persists almost unchanged (Figure 16a, dashed versus solid lines). The relative phasing of phytoplankton and microzooplankton at these model stations must be controlled not by the metabolic mechanisms *Rose and Caron* [2007] proposed, but rather by other aspects of the environment, perhaps the suddenness of ice-retreat-regulated spring blooms relative to those in ice-free conditions (Figures 12g and 16a). Furthermore, in the seasonal average, the model shows very little variation in the relationship between phytoplankton and microzooplankton production (Figure 16b): the latter is a near-constant fraction of the former. Microzooplankton appear to be tightly coupled to their prey even at the lowest temperatures observed in this system.

Other studies have suggested that the different temperature responses in autotrophs and heterotrophs will drive a restructuring of high-latitude ecosystems as those systems continue to warm. Many studies have found temperature sensitivity in zooplankton and marine bacteria to be higher than that of phytoplankton [*Pomeroy and Wiebe*, 2001; *Vaquer-Sunyer et al.*, 2010; *Chen et al.*, 2012], although the effective Q_{10} values of these sensitivities are highly variable and the commonly assumed difference between heterotroph and autotroph responses is not universally observed [*Robinson and Williams*, 1993]. (Some of the variability in these past results may arise from inappropriateness of the Q_{10} functional form as opposed to a linear [*Montagnes et al.*, 2003] or Arrhenius-type response [*Brown et al.*, 2004]; we have kept our analysis in terms of Q_{10} because of its familiarity.) The metabolic theory of ecology is also generally taken to predict a difference in temperature sensitivity between photosynthesis and respiration [*Brown et al.*, 2004; *López-Urrutia et al.*, 2006], and this hypothesis has motivated experimental studies [*Holding et al.*, 2013] and empirical and theoretical arguments that with ~5°C of warming, polar ecosystems pass a tipping point where respiration

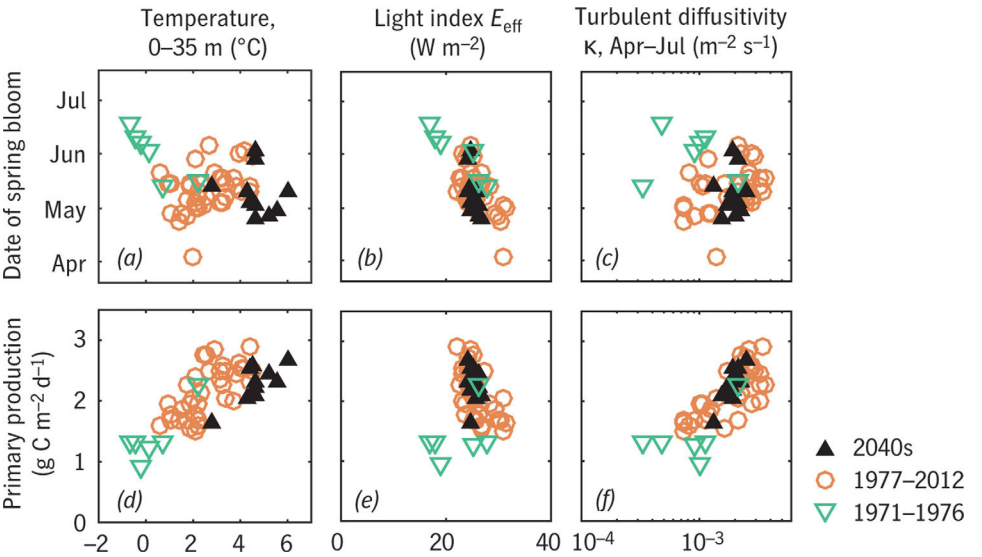

Figure 15. Modeled mean primary production and date of spring bloom in relation to selected environmental metrics at M2, for the 1971–1976 cold period (green, open triangles), 1979–2012 period (orange circles), and 2040s projection (black, solid triangles). Orange and green symbols together correspond to the orange symbols in Figure 12.

exceeds photosynthesis and carbon flows change fundamentally. A model like ours cannot test the ultimate validity of this "metabolic tipping point" hypothesis (i.e., whether the premise of a sensitivity difference is correct, or whether the conclusion of a tipping point accurately predicts the future), but the model does provide a framework in which we can impose the premise and test whether the conclusion follows, in EBS-like conditions.

Figure 17 shows results of two final ensembles of model cases in which the model was forced by spring 2009 conditions at M8 (a relatively cold year and location) and spring 2004 conditions at M2 (relatively warm conditions) under an array of combinations of Q_P and $Q_Z = Q_R$. A range of estimates of these parameters from the literature (converted where necessary from activation energies over −2°C–8°C) are shown for

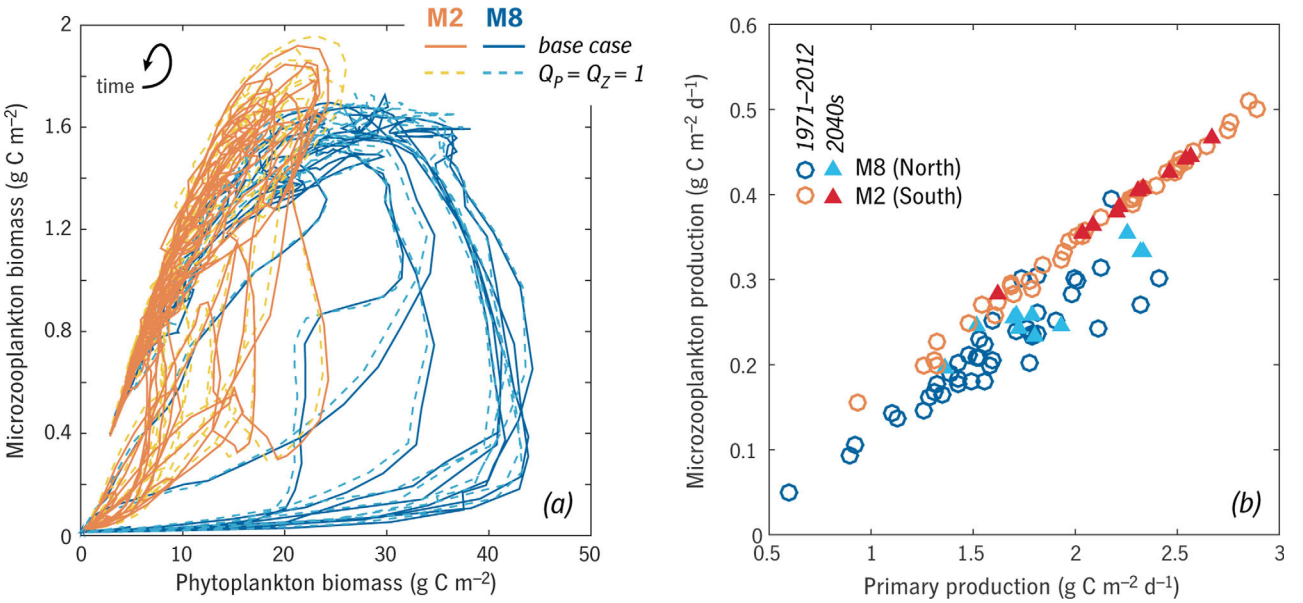

Figure 16. (a) Relative phasing of modeled phytoplankton and microzooplankton biomass, over the course of each hindcast spring at M2 (orange/yellow) and M8 (blue). Solid lines show the model base case, dashed lines the alternate $Q_P = Q_Z = Q_R = 1$ parameterization with direct effects of temperature omitted. Time from 15 February to 15 July runs generally counter-clockwise along these phase-space trajectories. (b) Relationship between primary and microzooplankton production across hindcast and projected future years at M2 and M8.

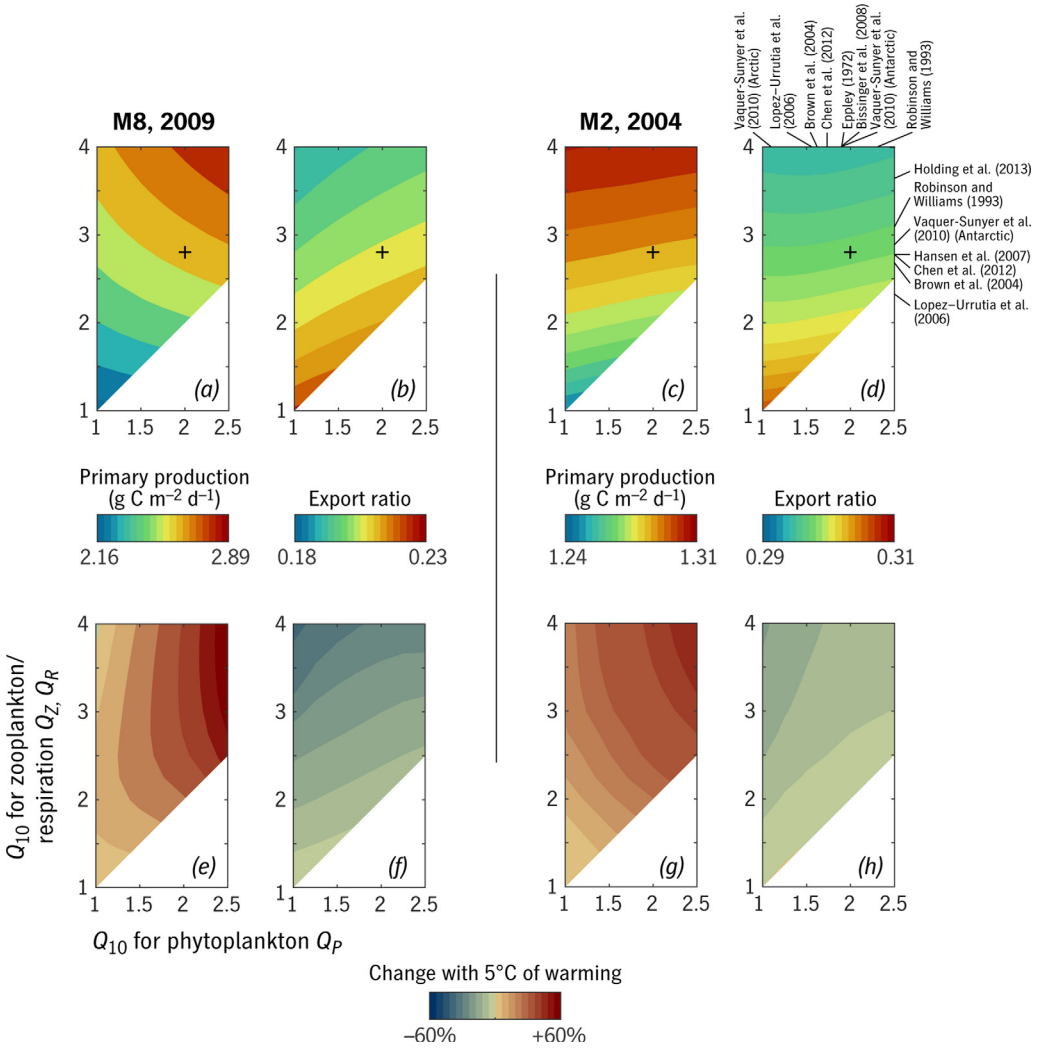

Figure 17. (a–d) Primary production and export ratio as functions of imposed Q_{10} values for phytoplankton and zooplankton, averaged 10 April to 15 July, for 2009 at M8 (relatively cold conditions) and 2004 at M2 (warm conditions). The model base case is marked with a plus. Literature estimates of Q_P and Q_Z are indicated at the margins of (d); one outlier ($Q_Z = 6.2$, the "Arctic" case reported by *Vaquer-Sunyer et al.* [2010]) is off the scale. Note the narrow range on the color scales. (e–h) As in Figures 17a–17d, but showing relative change in each metric between the case shown in Figures 17a–17d and a version in which temperature was uniformly raised 5°C.

comparison. As expected, as one moves from the balanced-response end of the parameter space ($Q_P \approx Q_Z$) to the high-Q_Z end, export ratio decreases (Figures 17b and 17d), suggesting a shift toward a recycling community fueled increasingly by regenerated nutrients. Primary production does not collapse under this increased grazing pressure but rather increases at both stations with increasing Q_Z, indicating that gains due to increased nutrient retention outweigh the direct losses to grazing. It is important to note the modest scale of the response of ecosystem function to Q_P, Q_Z: at M2 in 2004, for example, primary production only varies 6% over the entire parameter range.

To more directly address the hypothesis of a polar-ecosystems tipping point at 5°C of warming, we ran an additional set of cases which duplicate the hindcasts shown in Figures 17a–17d but with 5°C added uniformly (i.e., rate constants increased by $Q_P^{5/10}$, $Q_R^{5/10}$, $Q_Z^{5/10}$). Percent changes in the six metrics are shown in Figures 17e–17h. Results are consistent in direction with the sensitivity experiment in Figures 17a–17d: increasing grazing rate relative to maximum phytoplankton growth rate decreases export and increases mean primary production, to a modest degree (comparable to direct effects of temperature in the global models reviewed by *Laufkötter et al.* [2015]). None of the results here could be described as the passing of a tipping point in plankton productivity.

4. Discussion

4.1. Implications for Higher Trophic Levels

As discussed above, large interannual variation in the recruitment of pollock, salmon, and other pelagics have been linked to the relative abundance of lipid-rich zooplankton taxa in the EBS [*Hunt et al*., 2011; *Coyle et al*., 2011]. It remains an open question how exactly temperature, ice cover, and primary production magnitude and phenology combine to influence large zooplankton production, but this model study serves to narrow the likely hypotheses. In short, it appears much more likely that climate change shapes mesozooplankton production and composition through the timing of prey availability (both phytoplankton and microzooplankton) than through the overall magnitude of prey production. Over recent decades (1979–2012), our model suggests that total spring/early summer primary production has generally been higher in warmer years, opposite to the observed variation in large zooplankton [*Eisner et al*., 2014]. At the same time, the timing of the spring pelagic phytoplankton/microzooplankton bloom varies by a month or more between cold and warm years, in the model as in long-term observations (Figure 9), which is more than enough to have major interactions with copepod life histories [*Varpe et al*., 2007; *Ji et al*., 2010; *Mackas et al*., 2012]. A number of recent studies [*Søreide et al*., 2010; *Wassmann and Reigstad*, 2011; *Daase et al*., 2013] have suggested that this type of climate-linked phenological change could have critical impacts on the future recruitment success of large arctic/subarctic copepod taxa like *Calanus*, in which life history and reproductive strategy are closely tied to the spring bloom. Our model does not include in-ice algal production, which may be critical to large copepods in this system [*Durbin and Casas*, 2014] as in others [*Daase et al*., 2013]. If ice algal prey are available in February–March in cold years but not warm years in the southern EBS, this would further amplify the modeled interannual timing pattern (Figures 9 and 12a), and work against the variation in total production (Figure 12g).

4.2. Implications for the Metabolic Tipping-Point Hypothesis

We have argued that variation in spring bloom magnitude is modest on the interannual scale compared with phenological and other environmental variation. It is, of course, still possible that on a longer time scale, the planktonic ecosystem could prove to have a sigmoidal response to temperature [*Holding et al*., 2013], with the multidecadal warming trend leading to only small effects in the short term but driving the system past a tipping point at some point in the future. As discussed above, metabolic theory and recent observational and experimental studies have proposed exactly this. Our model strongly suggests that even if we grant the central premise—that respiration has a steeper temperature dependence than photosynthesis—the consequences may not be what the metabolic tipping-point hypothesis suggests (Figure 17). Even large variations in the temperature sensitivities of phytoplankton, zooplankton, and bacterial respiration drive only modest overall effects on primary and export production, and increasing zooplankton/bacterial rates actually increase total primary production in this model, rather than reducing it. For differences between phytoplankton and zooplankton Q_{10} values in the vicinity of the median prediction found in the literature (model base case; annotations, Figure 17b), we find that 5°C of warming is accompanied by a 20–30% increase in primary production.

Why would this model result be so different from, say, mesocosm studies of this topic such as *Holding et al*. [2013]? We speculate that the issue is the complexity of the biogeochemical role played by microzooplankton in a dynamic system where total primary production is controlled more by the physics of nutrient supply, as described above, than by grazing losses. It is true that the intense spring blooms seen in the northern EBS appear to involve a transient escape from grazer control (Figure 16a), but on longer and broader scales, it appears that nutrient regeneration by microzooplankton is actually essential to sustaining the bloom after nitrate is exhausted.

Even in several-month averages, *e*-ratio and *f*-ratio are highly imbalanced in this system (Figure 7), despite the close coupling of phytoplankton and their primary grazers (Figure 16). The nutrient budget of this wide shelf system takes a full seasonal cycle or more to close (C. Mordy, personal communication, 2014), and this may well be true for the primary production budget. We tentatively conclude that this ability to "evade gravity" for months at a time—nutrients ascend the water column and the trophic ladder and do not come down—is responsible for the result in which combinations of Q_{10} values that correspond to dramatic tipping points in other analyses produce nothing of the kind in modeled spring dynamics here. The lag time between peak rates of primary productivity and export appears to be similar in high-latitude [*Green and*

Sambrotto, 2006] and tropical [*Sambrotto*, 2001] systems, suggesting that the insensitivity of phytoplankton-microzooplankton interactions to temperature that we observe in the EBS may be a quite general pattern. This is a hypothesis that requires empirical, rather than numerical, exploration.

5. Summary and Conclusion

A new planktonic ecosystem model was constructed for the EBS based on diverse observations from the BEST/BSIERP field program: nitrate concentration, phytoplankton, and microzooplankton biomass, community growth, and grazing rates from dilution experiments, primary production rates from three other independent methods, and *f*-ratio from stable-isotope NO_3 and NH_4 uptake experiments. When run coupled to a data-assimilative ice-ocean hindcast of 1971–2012, the model performs well against in situ observations of spring bloom time-evolution and multiyear statistics of bloom timing, across a gradient of ice influence.

Capturing (1) the intensity of spring biomass accumulation at the northern IEB60 site in April–May and (2) the rapidity of the bloom's onset there while also capturing (3) the observed lack of a bloom at IEB60 during the partial ice retreat in March and (4) the delay of the spring bloom until May or June in ice-free conditions at M2 proved to be a major constraint on the model parameterization, especially given the additional constraints of (5) significant export out of the euphotic zone during spring and (6) significant microzooplankton grazing during the IEB60 bloom maximum (see section 3.1.1). To our knowledge, no other NPZ model has been shown to pass this precise of a multivariate test of bloom magnitude, timing, and internal dynamics at specific Bering Sea stations (or indeed to have been tested against such a data set). We have included a detailed set of metrics for the IEB60 test bed (Table 2) to encourage other modeling efforts to consider this mechanistically detailed benchmark along with spatially comprehensive but mechanistically ambiguous variables like chlorophyll.

This study examined only one projection of future climate, not an ensemble, and by a method that does not resolve indirect effects of global climate on the mesoscale atmospheric patterns that drive interannual variation in mixing and advection in the EBS. It captures, rather, the gross effect of the regional thermodynamic trend (imposed via a middle-of-the-road estimate of 8°C of air temperature increase by 2100) on surface water temperature and ice cover. Even as temperature in the southern EBS moves outside the range of historically observed conditions (Figure 2), the model projection does not find these novel combinations of temperature and ice cover, in themselves, to drive total spring primary production or spring bloom timing outside their historical ranges (Figure 15). This negative result required us to consider in detail whether temperature and ice cover, the most obvious indices of climate impacts on subarctic seas, are the right indices, or merely correlated historically with the right indices.

On the northern middle shelf, we found that ice cover straightforwardly controls spring bloom timing in the model; that bloom timing controls interannual variation in spring primary production; and that temperature and ice cover are correlated similarly across interannual and interdecadal scales (Figure 2). Thus, it is not particularly important—in a strictly predictive sense, on the northern shelf in particular—whether the individual sensitivities of phytoplankton to temperature, light, mixing, and so on are accurate or not in the model. In contrast, the dependencies proved to be more subtle on the southern middle shelf. The model hindcast suggests that bloom timing at M2 is controlled by surface (ice cover) and subsurface (turbulent mixing) effects on light availability in combination, as in the Oscillating Control Hypothesis [*Hunt et al.*, 2011]. It suggests that total spring primary production at M2 is controlled not by bloom timing as at M8 but by nutrient supply, with both advective transport and turbulent mixing contributing to interannual variation. (These patterns are summarized in Figure 18.) Crucially, both advection and wind mixing are processes that our future projection does not resolve trends in, and that global-scale climate models are not likely to predict accurately because of scale and their resolution of shelf processes.

These results are motivation for extremely careful spatial downscaling of climate projections in the Eastern Bering Sea, with particular attention to flushing, retention, and vertical mixing on the shelf. Advances in this area are very likely necessary even to determine whether total middle-shelf primary production in a warmer world is likely to be higher or lower than the present era. Accurate prediction of future trends in bloom timing is likely to also require advances in our conceptual and numerical models of plasticity in phytoplankton community light response, which turned out in this study to be both crucial and poorly constrained by

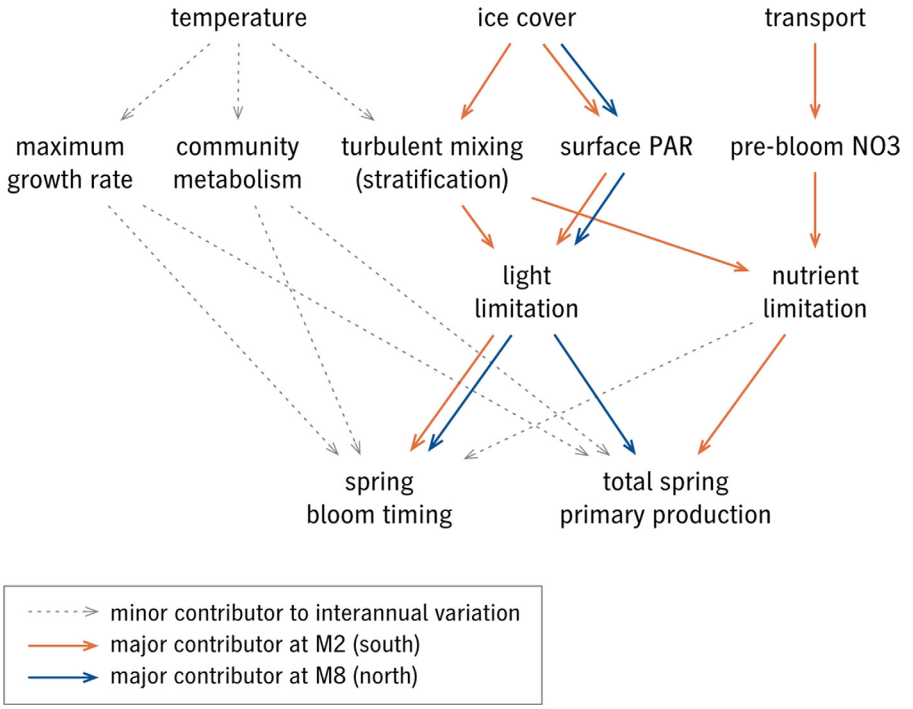

Figure 18. Summary of causal pathways from climate-linked environmental drivers to primary production magnitude and timing, for the northern middle shelf (M8) and southern middle shelf (M2), as diagnosed from the model hindcast (Figures 12–14). This summary applies to interannual-scale variation in spring/early summer processes in particular.

available data. Our solution—allowing α to vary as a function of a synthetic parameter that involves both surface light and subsurface mixing—is just one possibility among many. More generally, our numerical experiments regarding community metabolism suggest that similar issues may well arise across many other high-latitude systems, with direct effects of temperature on the plankton—although easier to conceptualize than plasticity in functional responses or regional shelf dynamics—proving to play a smaller role in future change than temperature's indirect, imperfect correlates.

Acknowledgments
This work was supported by the National Science Foundation through grants ARC-1107187, ARC-1107303, and ARC-1107588, for BEST Synthesis, and PLR-1417365. Many thanks to Phyllis Stabeno, Cal Mordy, and their research groups for providing essential observational data sets via the Bering Sea Project Data Archive and for aiding in their interpretation. N.S.B. would also like to thank Lisa Eisner, Steve Zeeman, Rolf Gradinger, Ned Cokelet, and George Hunt for helpful discussions. This is BEST-BSIERP Bering Sea Project publication number 179. All observational data used here are archived at *http://beringsea.eol.ucar.edu/*, and model output is available upon request.

References

Alcaraz, M., J. Felipe, U. Grote, E. Arashkevich, and A. Nikishina (2014), Life in a warming ocean: Thermal thresholds and metabolic balance of arctic zooplankton, *J. Plankton Res.*, *36*(1), 3–10.

Bagniewski, W., K. Fennel, M. J. Perry, and E. A. D'Asaro (2011), Optimizing models of the North Atlantic spring bloom using physical, chemical and bio-optical observations from a Lagrangian float, *Biogeosciences*, *8*(5), 1291–1307.

Banas, N. S., E. J. Lessard, R. M. Kudela, P. MacCready, T. D. Peterson, B. M. Hickey, and E. R. Frame (2009), Planktonic growth and grazing in the Columbia River plume region: A biophysical model study, *J. Geophys. Res.*, *114*, C00B06, doi:10.1029/2008JC004993.

Bissinger, J. E., D. Montagnes, J. Sharples, and D. Atkinson (2008), Predicting marine phytoplankton maximum growth rates from temperature: Improving on the Eppley curve using quantile regression, *Limnol. Oceanogr.*, *53*(2), 487–493.

Brown, J. H., J. F. Gillooly, A. P. Allen, V. M. Savage, and G. B. West (2004), Toward a metabolic theory of ecology, *Ecology*, *85*(7), 1771–1789.

Brown, Z. W., and K. R. Arrigo (2013), Sea ice impacts on spring bloom dynamics and net primary production in the Eastern Bering Sea, *J. Geophys. Res. Oceans*, *118*, 43–62, doi:10.1029/2012JC008034.

Campbell, R. G., C. J. Ashjian, E. B. Sherr, B. F. Sherr, M. W. Lomas, C. Ross, P. Alatalo, C. Gelfman, and D. Van Keuren (2016), Mesozooplankton grazing during spring sea-ice conditions in the eastern Bering Sea, *Deep Sea Res., Part II*, doi:10.1016/j.dsr2.2015.11.003, in press.

Chen, B., M. R. Landry, B. Huang, and H. Liu (2012), Does warming enhance the effect of microzooplankton grazing on marine phytoplankton in the ocean?, *Limnol. Oceanogr.*, *57*(2), 519–526.

Cianelli, D., M. R. D'Alcalà, V. Saggiomo, and E. Zambianchi (2004), Coupling mixing and photophysiological response of Antarctic plankton: A Lagrangian approach, *Antarct. Sci.*, *16*(2), 133–142.

Coachman, L. K. (1986), Circulation, water masses, and fluxes on the southeastern Bering Sea shelf, *Cont. Shelf Res.*, *5*, 23–108.

Collos, Y., A. Vaquer, and P. Souchu (2005), Acclimation of nitrate uptake by phytoplankton to high substrate levels, *J. Phycol.*, *41*(3), 466–478.

Cooper, L. W., M. G. Sexson, J. M. Grebmeier, R. Gradinger, C. W. Mordy, and J. R. Lovvorn (2013), Linkages between sea-ice coverage, pelagic-benthic coupling, and the distribution of spectacled eiders: Observations in March 2008, 2009 and 2010, northern Bering Sea, *Deep Sea Res., Part II*, *94*, 31–43.

Coyle, K. O., L. B. Eisner, F. J. Mueter, A. I. Pinchuk, M. A. Janout, K. D. Cieciel, E. V. Farley, and A. G. Andrews (2011), Climate change in the southeastern Bering Sea: Impacts on pollock stocks and implications for the oscillating control hypothesis, *Fish. Oceanogr.*, *20*(2), 139–156.

Cross, J. N., J. T. Mathis, and N. R. Bates (2012), Hydrographic controls on net community production and total organic carbon distributions in the eastern Bering Sea, *Deep Sea Res., Part II*, *65-70*(C), 98–109.
Daase, M., S. Falk-Petersen, Ø. Varpe, G. Darnis, J. E. Søreide, A. Wold, E. Leu, J. Berge, B. Philippe, and L. Fortier (2013), Timing of reproductive events in the marine copepod Calanus glacialis: A pan-Arctic perspective, *Can. J. Fish. Aquat. Sci.*, *70*, 871–884.
Danielson, S., L. Eisner, T. Weingartner, and K. Aagaard (2011a), Thermal and haline variability over the central Bering Sea shelf Seasonal and interannual perspectives, *Cont. Shelf Res.*, *31*(6), 539–554.
Danielson, S., E. Curchitser, K. Hedstrom, T. Weingartner, and P. Stabeno (2011b), On ocean and sea ice modes of variability in the Bering Sea, *J. Geophys. Res.*, *116*, C12034, doi:10.1029/2011JC007389.
Dukowicz, J. K., and R. D. Smith (1994), Implicit free-surface method for the Bryan-Cox-Semtner ocean model, *J. Geophys. Res.*, *99*(C4), 7991–8014.
Durbin, E. G., and M. C. Casas (2014), Early reproduction by Calanus glacialis in the Northern Bering Sea: The role of ice algae as revealed by molecular analysis, *J. Plankton Res.*, *36*(2), 523–541.
Eisner, L. B., J. M. Napp, K. L. Mier, A. I. Pinchuk, and A. G. Andrews (2014), Climate-mediated changes in zooplankton community structure for the eastern Bering Sea, *Deep Sea Res., Part II*, *109*, 157–171.
Fasham, M. J. R., K. J. Flynn, P. Pondaven, T. R. Anderson, and P. W. Boyd (2006), Development of a robust marine ecosystem model to predict the role of iron in biogeochemical cycles: A comparison of results for iron-replete and iron-limited areas, and the SOIREE iron-enrichment experiment, *Deep Sea Res., Part I*, *53*(2), 333–366.
Flato, G. M., and W. D. Hibler (1995), Ridging and strength in modeling the thickness distribution of Arctic sea ice, *J. Geophys. Res.*, *100*(C9), 18,611–18,626.
Franzè, G., and P. J. Lavrentyev (2014), Microzooplankton growth rates examined across a temperature gradient in the Barents Sea, *PloS one*, *9*(1), e86,429.
Gentleman, W., A. W. Leising, B. W. Frost, S. L. Strom, and J. Murray (2003), Functional responses for zooplankton feeding on multiple resources: A review of assumptions and biological dynamics, *Deep Sea Res., Part II*, *50*(22-26), 2847–2875.
Grebmeier, J. M., J. E. Overland, S. E. Moore, E. V. Farley, E. C. Carmack, L. W. Cooper, K. E. Frey, J. H. Helle, F. A. McLaughlin, and S. L. McNutt (2006), A major ecosystem shift in the northern Bering Sea, *Science*, *311*(5766), 1461–1464.
Green, S. E., and R. N. Sambrotto (2006), Plankton community structure and export of C, N, P and Si in the Antarctic Circumpolar Current, *Deep Sea Res., Part II*, *53*(5-7), 620–643.
Hansen, J., P. K. Bjornsen, and B. W. Hansen (1997), Zooplankton grazing and growth: Scaling within the 2–2,000 μm body size range, *Limnol. Oceanogr.*, *42*(4), 687–704.
Hibler, W. D. (1980), Modeling a variable thickness sea ice cover, *Mon. Weather Rev.*, *108*(12), 1943–1973.
Holding, J. M., C. M. Duarte, and J. M. Arrieta (2013), Experimentally determined temperature thresholds for Arctic plankton community metabolism, *Biogeosciences*, *10*, 357–370.
Hunt, G. L., Jr., P. J. Stabeno, G. Walters, E. Sinclair, R. D. Brodeur, J. M. Napp, and N. A. Bond (2002), Climate change and control of the southeastern Bering Sea pelagic ecosystem, *Deep Sea Res., Part II*, *49*, 5821–5853.
Hunt, G. L., Jr., et al. (2011), Climate impacts on eastern Bering Sea foodwebs: A synthesis of new data and an assessment of the Oscillating Control Hypothesis, *ICES J. Mar. Sci.*, *68*(6), 1230–1243.
IPCC (2007), *Climate Change 2007: The Physical Science Basis. Contribution of Working Group I to the Fourth Assessment Report of the Intergovernmental Panel on Climate Change*, Cambridge Univ. Press, Cambridge, U. K.
Ji, R., M. Edwards, D. L. Mackas, J. A. Runge, and A. C. Thomas (2010), Marine plankton phenology and life history in a changing climate: Current research and future directions, *J. Plankton Res.*, *32*(10), 1355–1368.
Kalnay, E., et al. (1996), The NCEP/NCAR 40-year reanalysis project, *Bull. Am. Meteorol. Soc.*, *77*(3), 437–471.
Ladd, C., and N. A. Bond (2002), Evaluation of the NCEP/NCAR reanalysis in the NE Pacific and the Bering Sea, *J. Geophys. Res.*, *107*(C10), 3158, doi:10.1029/2001JC001157.
Ladd, C., and P. J. Stabeno (2012), Stratification on the Eastern Bering Sea shelf revisited, *Deep Sea Res., Part II*, *65-70*, 72–83.
Laufkötter, C., et al. (2015), Drivers and uncertainties of future global marine primary production in marine ecosystem models, *Biogeosciences*, *12*, 6955–6984.
Lindsay, R. W., and J. Zhang (2006), Assimilation of ice concentration in an ice–ocean model, *J. Atmos. Oceanic Technol.*, *25*, 742–749.
Lomas, M. W., S. B. Moran, J. R. Casey, D. W. Bell, M. Tiahlo, J. Whitefield, R. P. Kelly, J. T. Mathis, and E. D. Cokelet (2012), Spatial and seasonal variability of primary production on the Eastern Bering Sea shelf, *Deep Sea Res., Part II*, *65-70*, 126–140.
López-Urrutia, Á., E. S. Martin, R. P. Harris, and X. Irigoien (2006), Scaling the metabolic balance of the oceans, *Proc. Natl. Acad. Sci. U. S. A.*, *103*(23), 8739–8744.
Mackas, D. L., et al. (2012), Changing zooplankton seasonality in a changing ocean: Comparing time series of zooplankton phenology, *Prog. Oceanogr.*, *97-100*, 31–62.
Miksis-Olds, J. L., P. J. Stabeno, J. M. Napp, A. I. Pinchuk, J. A. Nystuen, J. D. Warren, and S. L. Denes (2013), Ecosystem response to a temporary sea ice retreat in the Bering Sea: Winter 2009, *Prog. Oceanogr.*, *111*, 38–51.
Montagnes, D., S. A. Kimmance, and D. Atkinson (2003), Using Q10: Can growth rates increase linearly with temperature?, *Aquat. Microbial Ecol.*, *32*(3), 307–313.
Mordy, C. W., P. J. Stabeno, E. D. Cokelet, C. Ladd, F. A. Menzia, P. Proctor, and E. Wisegarver (2012), Net community production on the middle shelf of the eastern Bering Sea, *Deep Sea Res., Part II*, *65-70*, 110–125.
Pahlow, M., and A. Oschlies (2013), Optimal allocation backs Droop's cell-quota model, *Mar. Ecol. Prog. Ser.*, *473*, 1–5.
Palmer, M. A., K. R. Arrigo, C. J. Mundy, J. K. Ehn, M. Gosselin, D. G. Barber, J. Martin, E. Alou, S. Roy, and J.-É. Tremblay (2011), Spatial and temporal variation of photosynthetic parameters in natural phytoplankton assemblages in the Beaufort Sea, Canadian Arctic, *Polar Biol.*, *34*, 1915–1928.
Pomeroy, L. R., and W. J. Wiebe (2001), Temperature and substrates as interactive limiting factors for marine heterotrophic bacteria, *Aquat. Microbial Ecol.*, *23*, 187–204.
Robinson, C., and P. J. L. Williams (1993), Temperature and Antarctic plankton community respiration, *J. Plankton Res.*, *15*, 1035–1051.
Rodionov, S. N., N. A. Bond, and J. E. Overland (2007), The Aleutian Low, storm tracks, and winter climate variability in the Bering Sea, *Deep Sea Res., Part II*, *54*(23-26), 2560–2577.
Rose, J. M., and D. A. Caron (2007), Does low temperature constrain the growth rates of heterotrophic protists? Evidence and implications for algal blooms in cold waters, *Limnol. Oceanogr.*, *52*(2), 886–895.
Sambrotto, R. N. (2001), Nitrogen production in the northern Arabian Sea during the Spring Intermonsoon and Southwest Monsoon seasons, *Deep Sea Res., Part II*, *48*(6-7), 1173–1198.

Sambrotto, R. N., H. J. Niebauer, and J. J. Goering (1986), Relationships among vertical mixing, nitrate uptake, and phytoplankton growth during the spring bloom in the southeast Bering Sea middle shelf, *Cont. Shelf Res.*, *5*(1/2), 161–198.
Sambrotto, R. N., D. Burdloff, and K. McKee (2016), Spatial and year-to-year patterns in new and primary productivity in sea ice melt regions of the eastern Bering Sea, *Deep Sea Res., Part II*, doi:10.1016/j.dsr2.2015.07.011, in press.
Sherr, E. B., and B. F. Sherr (2009), Capacity of herbivorous protists to control initiation and development of mass phytoplankton blooms, *Aquat. Microbial Ecol.*, *57*, 253–262.
Sherr, E. B., B. F. Sherr, and C. Ross (2013), Microzooplankton grazing impact in the Bering Sea during spring sea ice conditions, *Deep Sea Res., Part II*, *94*, 57–67.
Sigler, M. F., P. J. Stabeno, L. B. Eisner, J. M. Napp, and F. J. Mueter (2014), Spring and fall phytoplankton blooms in a productive subarctic ecosystem, the eastern Bering Sea, during 1995–2011, *Deep Sea Res., Part II*, *109*, 71–83.
Smith, R. D., J. K. Dukowicz, and R. C. Malone (1992), Parallel ocean general circulation modeling, *Physica D*, *60*(1-4), 38–61.
Smith, S. L., Y. Yamanaka, M. Pahlow, and A. Oschlies (2009), Optimal uptake kinetics: Physiological acclimation explains the pattern of nitrate uptake by phytoplankton in the ocean, *Mar. Ecol. Prog. Ser.*, *384*, 1–13.
Søreide, J. E., E. Leu, J. Berge, M. Graeve, and S. Falk-Petersen (2010), Timing of blooms, algal food quality and Calanus glacialis reproduction and growth in a changing Arctic, *Global Change Biol.*, *16*, 3154–3163.
Stabeno, P. J., N. B. Kachel, S. Moore, J. M. Napp, M. F. Sigler, A. Yamaguchi, and A. N. Zerbini (2012a), Comparison of warm and cold years on the southeastern Bering Sea shelf and some implications for the ecosystem, *Deep Sea Res., Part II*, *65-70*(C), 31–45.
Stabeno, P. J., E. V. Farley Jr., N. B. Kachel, S. Moore, C. W. Mordy, J. M. Napp, J. E. Overland, A. I. Pinchuk, and M. F. Sigler (2012b), A comparison of the physics of the northern and southern shelves of the eastern Bering Sea and some implications for the ecosystem, *Deep Sea Res., Part II*, *65-70*, 14–30.
Stoecker, D. K., A. Weigel, and J. I. Goes (2013a), Microzooplankton grazing in the Eastern Bering Sea in summer, *Deep Sea Res., Part II*, *109*, 145–156.
Stoecker, D. K., A. C. Weigel, D. A. Stockwell, and M. W. Lomas (2013b), Microzooplankton: Abundance, biomass and contribution to chlorophyll in the Eastern Bering Sea in summer, *Deep Sea Res., Part II*, *109*, 134–144.
Thorndike, A. S., D. A. Rothrock, G. A. Maykut, and R. Colony (1975), The thickness distribution of sea ice, *J. Geophys. Res.*, *80*(33), 4501–4513.
Vaquer-Sunyer, R., C. M. Duarte, R. Santiago, P. Wassmann, and M. Reigstad (2010), Experimental evaluation of planktonic respiration response to warming in the European Arctic Sector, *Polar Biol.*, *33*, 1661–1671.
Varpe, Ø., C. Jørgensen, G. A. Tarling, and Ø. Fiksen (2007), Early is better: Seasonal egg fitness and timing of reproduction in a zooplankton life-history model, *Oikos*, *116*(8), 1331–1342.
Wang, M., J. E. Overland, and P. Stabeno (2012), Future climate of the Bering and Chukchi Seas projected by global climate models, *Deep Sea Res., Part II*, *65-70*(C), 46–57.
Ward, B. A., M. Schartau, A. Oschlies, and A. P. Martin (2013), When is a biogeochemical model too complex? Objective model reduction and selection for North Atlantic time-series sites, *Prog. Oceanogr.*, *116*, 49–65.
Wassmann, P., and M. Reigstad (2011), Future Arctic Ocean seasonal ice zones and implications for pelagic-benthic coupling, *Oceanography*, *24*(3), 220–231.
Wiese, F. K., T. I. Van Pelt, and W. J. Wiseman (2012), Bering Sea linkages, *Deep Sea Res., Part II*, *65-70*, 2–5.
Willmott, C. J. (1981), On the validation of models, *Phys. Geogr.*, *2*(2), 181–194.
Zeeman, S. J., and P. R. Jensen (1990), Photoresponses of phytoplankton in the Bering Sea, in *Results of the Second Joint U.S.-U.S.S.R. Bering Sea Expedition, Summer 1984*, edited by P. F. Roscigno, pp. 87–96, U.S. Dep. of the Inter, Washington, D. C.
Zhang, J. (2005), Warming of the arctic ice-ocean system is faster than the global average since the 1960s, *Geophys. Res. Lett.*, *32*, L19602, doi:10.1029/2005GL024216.
Zhang, J., and W. D. Hibler (1997), On an efficient numerical method for modeling sea ice dynamics, *J. Geophys. Res.*, *102*(C4), 8691–8702.
Zhang, J., and D. Rothrock (2001), A thickness and enthalpy distribution sea-ice model, *J. Phys. Oceanogr.*, *31*(10), 2986–3001.
Zhang, J., and D. A. Rothrock (2005), Effect of sea ice rheology in numerical investigations of climate, *J. Geophys. Res.*, *110*, C08014, doi:10.1029/2004JC002599.
Zhang, J., R. Woodgate, and R. Moritz (2010a), Sea ice response to atmospheric and oceanic forcing in the Bering Sea, *J. Phys. Oceanogr.*, *40*(8), 1729–1747.
Zhang, J., P. A. Matrai, Y. H. Spitz, M. Steele, C. J. Ashjian, R. G. Campbell, and L. Berline (2010b), Modeling the impact of declining sea ice on the Arctic marine planktonic ecosystem, *J. Geophys. Res.*, *115*, C10015, doi:10.1029/2009JC005387.
Zhang, J., R. Woodgate, and S. Mangiameli (2012), Towards seasonal prediction of the distribution and extent of cold bottom waters on the Bering Sea shelf, *Deep Sea Res., Part II*, *65-70*, 58–71.